JGR Atmospheres

RESEARCH ARTICLE
10.1029/2022JD036563

Key Points:

- The Noah-MP LSM leads to a more accurate size distribution and growth rate of convection compared to the Noah LSM
- The latent and sensible heating components of the surface radiation balance drive differences in local circulation patterns
- Surface energy imbalances impact updraft characteristics, leading to downstream influences of cloud growth and sustained convection

Correspondence to:
D. S. Henderson,
dshenderson@wisc.edu

Citation:
Henderson, D. S., Otkin, J. A., & Mecikalski, J. R. (2022). Examining the role of the land surface on convection using high-resolution model forecasts over the Southeastern United States. *Journal of Geophysical Research: Atmospheres*, *127*, e2022JD036563. https://doi.org/10.1029/2022JD036563

Received 27 JAN 2022
Accepted 25 JUL 2022

© 2022. The Authors.
This is an open access article under the terms of the Creative Commons Attribution-NonCommercial License, which permits use, distribution and reproduction in any medium, provided the original work is properly cited and is not used for commercial purposes.

Examining the Role of the Land Surface on Convection Using High-Resolution Model Forecasts Over the Southeastern United States

David S. Henderson[1], Jason A. Otkin[1,2], and John R. Mecikalski[3]

[1]Space Science and Engineering Center, University of Wisconsin-Madison, Madison, WI, USA, [2]Cooperative Institute for Meteorological Satellite Studies, University of Wisconsin-Madison, Madison, WI, USA, [3]Department of Atmospheric Sciences, University of Alabama in Huntsville, Huntsville, AL, USA

Abstract The influence of the Unified Noah and Noah-MP land surface models (LSMs) on the evolution of cumulus clouds reaching convective initiation (CI) is assessed using infrared brightness temperatures (BT) from GOES-16. Cloud properties from individual cloud objects are examined using output from high-resolution (500 m horizontal grid spacing) model simulations. Cloud objects are tracked over time and related to observed clouds reaching CI to examine differences in cloud extent, longevity, and growth rate. The results demonstrate that differences in assumed surface properties can lead to large discrepancies in the net surface radiative budget, particularly in the sensible and latent heating components where differences exceed 40 W m^{-2}. These differences lead to changes in the local mesoscale circulation patterns that are more pronounced near the edges of forested and grassland boundaries where lower-level convergence is stronger. Higher sensible heating from the Noah-MP LSM produced growth of CI clouds earlier and with increased longevity, which was closer to the timing and growth observed from GOES-16. The increased cloud growth in the Noah-MP experiment results from stronger and deeper updrafts, which lofts more cloud water into the upper levels of the troposphere. The weaker updrafts from the Noah LSM experiment results in shallower convection after CI is detected due to slower growth rates. The differences in cloud properties and growth are directly related to the land surfaces they develop above and point to the importance of accurately representing land properties and radiative characteristics when simulating convection in numerical weather prediction models.

Plain Language Summary Weather prediction models consist of many different parameters and assumptions. In this study, we compared how assumptions of the land surface impact the growth of cumulus clouds and thunderstorms across the southeastern United States. It was found that differences in the land surface schemes can directly impact the local circulations where cumulus clouds and convective storms develop; this leads to differences in how large the clouds grow and sustain over time. By tracking clouds using an object-based methodology, we were able to compare growth characteristics to those observed by geostationary satellites. The model and satellite comparisons helped demonstrate that the cloud growth is quite sensitive to the model interpretation of surface energy balances, particularly over heterogeneous landscapes containing forests and grasslands. The differences in the amount of energy transferred from the surface to the atmosphere lead to downstream differences in cloud updraft strength. These differences in cumulus cloud characteristics influence the formation of ice in the upper levels of clouds, which is essential in the convective storm initiation process. The comparison with satellite data provided the ability to validate cloud growth and further understand the processes leading to longer-lived thunderstorms.

1. Introduction

Land surface processes are key in regulating regional sources of energy and moisture, which may significantly impact the timing and spatial evolution of convection and precipitation. For example, in the Southeastern United States, land surface heterogeneity characterized by adjacent areas of forests, grassland, and cropland is a factor in determining regional initiation of convection (Gambill & Mecikalski, 2011). Understanding the processes impacting cumulus clouds that undergo the convective initiation (CI) process is essential as the development of isolated convective clouds during summer months are driven primarily by strong surface heating in weakly forced environments (Brown & Arnold, 1998; Gambill & Mecikalski, 2011; Kirshbaum et al., 2016; Miller &

Mote, 2017). Over large regions of the Southeast United States, these storms make up a significant portion of the spring and summer seasonal precipitation totals (Rickenbach et al., 2020).

The Southeast United States poses an especially challenging forecast problem related to CI and the upscale development of convective storms. CI forecasting is particularly challenging during the summer when synoptic scale forcing is typically weak, solar heating is strong, surface moisture is abundant, and given high land surface heterogeneity (i.e., forests intermingled with farmland and small water bodies). Prediction of the onset time, location, and evolution of convection remains a difficult problem for observational and numerical weather prediction (NWP) models (e.g., Cintineo et al., 2020; Henderson et al., 2021; Kain et al., 2013; Lawson et al., 2018; Mecikalski et al., 2015). Studies by Gambill and Mecikalski (2011) and Asefi et al. (2012) show that heterogeneous land cover and small lakes significantly influence summertime convective cloud development and storm initiation in the Southeastern United States. A heterogeneous landscape coupled to weak winds in synoptically tranquil environments ($\leq$5 m s^{-1} surface and 500 hPa winds <7.5 m s^{-1} winds; Brown & Arnold, 1998) leads to the formation of differential heating-generated mesoscale circulations that in turn help buoyant thermal updrafts reach the level of free convection (LFC) in advance of CI, especially when surface dew points are high ($\geq$22–27°C; Carlton et al., 2008; Trier et al., 2004; Wilson & Schreiber, 1986). In these environments, there is a close coupling between the land surface and convective storm development, which is often dictated by local vegetation, land cover, antecedent rainfall, and topography features that generate the differential heating circulations (Avissar & Schmidt, 1998; Walker et al., 2009). As synoptic scale wind velocities increase, these differential heating-generated circulations become more organized linear features that cause cloud streets and horizontal convective rolls (Avissar & Schmidt, 1998; LeMone, 1973). Because of the sensitivity of CI to land cover and land use, and of CI related to cloud microphysical schemes (Henderson et al., 2021), convection allowing NWP models often fail to resolve the subtle factors that lead to the development of convective storms in the Southeastern United States. An accurate depiction of the land characteristics and land surface interactions with the atmosphere becomes essential to predict cloud formation over regions with complex variations in vegetation and weak atmospheric flow.

Differences in the treatment of land and vegetation processes in land surface models (LSMs) impact surface sensible and latent heat fluxes, convective mixing, boundary layer growth, and the transport of moisture into the upper troposphere (e.g., Anthes, 1984; Duda et al., 2017; Pielke, 2001; Santanello et al., 2018). Modeling-based studies have examined the interactions between the land surface and the atmosphere to discuss land impacts on downstream cloud growth (e.g., García-García et al., 2021; Kirkpatrick et al., 2011; Knist et al., 2020; PaiMazumder et al., 2012; Pei et al., 2014) and LSM perturbation studies can be used to gauge the impacts of systematic changes in land surface properties (Deng et al., 2016; Duda et al., 2017; Orth et al., 2016; Zhu et al., 2018). Ground-based observational studies have examined the land-atmosphere coupling conditions leading to deep convection (e.g., Lareau, 2020; Qiu & Williams, 2020; Van Weverberg et al., 2018; Zhang & Klein, 2010) and high temporal resolution data from geostationary satellites have also been used to better understand the processes leading to CI (Bikos et al., 2012; Griffin et al., 2021; Henderson et al., 2021; Mecikalski et al., 2015; Senf & Deneke, 2017). Geostationary satellites, however, are unable to observe below the cloud top due to signal saturation, resulting in a disconnect to the cloud and atmosphere below. Further, the aforementioned model and ground-based studies lack conclusions on the quantitative effects of the different types of land surface heterogeneity.

The high-temporal-resolution data from the GOES-16 Advanced Baseline Imager (ABI; Schmit et al., 2017) provides an ideal data set to track the life cycle of convection. The temporal resolution of 1–5 min allows validation on scales of cumulus cloud growth (Gravelle et al., 2016). The object tracking methodology and validation strategies employed during this study are consistent with observation-based tracking techniques used to describe CI characteristics and nowcasting studies (e.g., Harris et al., 2010; Mecikalski et al., 2010; 2016; Senf & Deneke, 2017). This has been shown to provide beneficial information in CI nowcasting applications (Mecikalski et al., 2015; Patou et al., 2018). Using the 5-min temporal-resolution data from the GOES-16 ABI, Henderson et al. (2021) applied cloud object tracking methods to examine the growth of individual convective cells produced by high-resolution Weather Research and Forecasting (WRF; Powers et al., 2017) model simulations to understand how bulk microphysical parameterization schemes represent the formation and development of hydrometeor species, cloud growth, and precipitation processes. The study showed that while the microphysical parameterization schemes produce varying magnitudes of hydrometeor mixing ratios (i.e., cloud water,

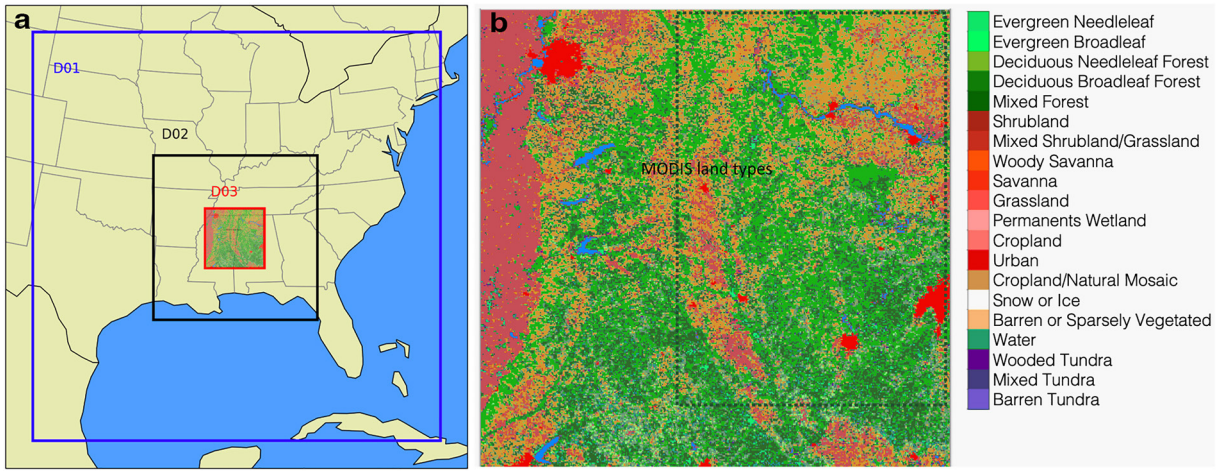

Figure 1. (a) The three Weather Research and Forecasting Model domains used in the land surface model experiments. Convective initiation is assessed within the inner domain (D03). (b) The MODIS land use classes on D03.

ice, and precipitation), the schemes agreed in the processes leading to CI when evaluating clouds with similar observed IR BT growth rates.

The overall goal of this work is to examine how the LSM and land-atmosphere interactions influence cloud extent, longevity, updrafts, and in-cloud microphysics for convection reaching CI. Specifically, we use geostationary satellite data in conjunction with high-resolution WRF model simulations to validate cloud growth in the model. This work expands upon the results from Henderson et al. (2021) to shed light on other factors controlling the growth of convection to better understand the conditions optimal for CI occurrence and upscale storm growth in weakly forced scenarios. The work concentrates on how the use of different LSMs leads to changes in the overall net surface radiative budget and the respective impact on convective growth and updraft characteristics. CI from high-resolution simulations is evaluated using lag-based composites of cloud objects as a function of the timing of CI to track individual convective cells. Comparing observed and simulated GOES-16 ABI imagery focuses on the model's ability to simulate the evolution of convection independent of the cloud location and time. The object-based evaluation is applied to gain greater understanding of the relationships between the land surface, the surface radiation budget, and their respective downstream influences on atmospheric motion and cloud growth.

This study is organized as follows. In Section 2, we briefly describe each data set, model experiment setup, and methods used to track clouds. In Section 3, we evaluate and discuss the differences in CI and storm evolution between the Unified Noah and Noah with Multiple Parameterizations (Noah-MP) LSMs. After that, we then document the physical differences occurring in convection leading to discrepancies in cloud growth. Finally, a summary and discussion are given in Section 4.

2. Methods

2.1. Model Setup

This work expands upon the Henderson et al. (2021) case study from May 20, 2018 that used WRF model version 3.9.1.1 to examine convection over the Southeastern United States (Figure 1). This event was characterized by weakly forced, slow-moving convective features that occurred across Alabama and Mississippi during the afternoon and evening hours. The model configuration consists of three two-way feedback permitted nests with 12.5 km, 2.5 km, and 500 m resolution, respectively (Figure 1). The innermost domain contains 700 × 700 horizontal grid points with 53 vertical sigma levels and a model top of 25 hPa. The initial and lateral boundary conditions are provided by the National Centers for Environmental Prediction final (NCEP FNL) analyses with a 6-hr temporal resolution on a 0.25° latitude-longitude grid.

The model setup was derived through a series of sensitivity experiments (not shown) that examined the impacts of using different microphysical schemes, planetary boundary layer (PBL) schemes, and model spin-up time on the results. The chosen configuration below provides the most accurate representation of the cloud evolution during this event when compared to the GOES-16 ABI observations. The two simulations evaluated in this study are initialized at 1200 UTC, allowing for ∼5 hr of spin-up before CI occurs, and contain an identical model configuration apart from the LSM. The data is output every 5 min, which matches the temporal resolution of the GOES-16 ABI observations. The Thompson cloud microphysics scheme (Thompson et al., 2008) is used along with the Rapid Radiative Transfer Model for Global Climate Models (RRTMG; Iacono et al., 2008) longwave and shortwave radiation schemes. The Thompson microphysics scheme is used because Henderson et al. (2021) concluded that it provided the most accurate cloud growth rates and evolution of cloud top ice microphysics during the case study examined. The Tiedtke (Tiedtke, 1989; Zhang et al., 2011) cumulus parameterization scheme is used only on the outermost domain. Though Henderson et al. (2021) employed the Yonsei University (YSU; Hong et al., 2006; Lim & Hong, 2010) PBL scheme, here we use the Mellor-Yamanda-Nakanishi-Niino (MYNN; Nakanishi & Niino, 2004, 2009) 2.5-level closure PBL scheme. Utilizing the MYNN PBL scheme yielded more accurate cloud growth when compared to GOES-16 in our sensitivity analysis and has showed better PBL evolution in convection-allowing models (e.g., Coniglio et al., 2013). We note, however, that changes in the LSM resulted in a larger impact on cloud evolution compared to the PBL scheme, which is a similar finding to Griffin et al. (2021).

To assess the impact of the land surface on CI, two WRF sensitivity experiments are performed using the Noah and Noah-MP LSMs with the above configuration. The Noah LSM contains four soil layers and combines a surface layer of vegetation and soil surface, which makes it applicable in both operational weather and climate models (Barlage et al., 2010; Ek et al., 2003). When moving toward higher resolution, representation of the land surface becomes increasingly important (e.g., Case et al., 2008; Sutton et al., 2006). The Noah-MP LSM expands upon the Noah model by providing a highly configurable LSM with numerous options to represent groundwater and vegetation processes. The Noah-MP LSM provides a multi-layer snow pack, explicit representation of surface water infiltration runoff and groundwater transfer, and adds a physical canopy layer with explicit radiative transfer interactions between the surface and canopy. The canopy layer is separated from the surface, which improves the representation of the surface energy balance (i.e., solar radiation, longwave radiation, sensible heat, latent heat, and ground heat fluxes). This allows the Noah-MP model to compute the canopy temperature, and related radiative energy, water, and carbon fluxes explicitly between the surface and canopy and the canopy to the overlying atmosphere (Niu et al., 2011). For this work, we utilize the default recommended options for different parameterizations available in WRF V3.9.1.1. This includes static vegetation (dynamics option 5). Static vegetation helps focus the differences between the Noah and Noah-MP LSMs on the representation of land surface types and canopy radiative transfer from the Noah-MP LSM. We note that for this case study, the maximum vegetation fraction used by the recommended dynamics option does not alter the overall results compared to a climatological vegetation fraction (dynamics option 1). Further discussion of the vegetation fraction can be found in Section 4.

2.2. Cloud Tracking

2.2.1. Observed and Simulated Brightness Temperatures

The verification data set is observed BTs from the GOES-16 ABI sensor (Schmit et al., 2017). This analysis uses the 10.35 μm BTs, which have a 2-km pixel spacing at nadir at 5-min time intervals. Similar to previous methodologies (e.g., Griffin et al., 2017, 2021; Henderson et al., 2021), the Community Radiative Transfer Model version 2.1 (CRTM; Ding et al., 2011) is used to generate simulated GOES-16 ABI IR BT data from the WRF simulations. The CRTM provides all-sky top-of-the-atmosphere BTs that incorporate the viewing geometry for the GOES-16 ABI. For cloudy grid points, an effective radius consistent with the assumptions made by the Thompson microphysics scheme (Otkin et al., 2007; Thompson et al., 2016) is diagnosed for each species (cloud water, rainwater, ice, snow, and graupel) and then input along with the hydrometeor mixing ratios to the CRTM. The CRTM then computes cloud optical properties (i.e., single scatter albedo, asymmetry parameter, and full scattering phase function) for each grid point and vertical layer. Finally, the combined set of cloud optical properties is used to compute the simulated IR BTs on the 500 m resolution grid, which is then averaged to the 2-km resolution GOES-16 ABI grid to maintain consistency with the ABI observations.

2.2.2. Cloud Tracking and Compositing Data

The cloud tracking procedure for the observed and simulated BT data sets follows the method described in Henderson et al. (2021) and is summarized briefly here. The physical basis for the tracking method is derived using the Tracking Of Organized Convection Algorithm through 3D segmentation (TOOCAN; Fiolleau & Roca, 2013) algorithm with clouds tracked through time when overlapping cloud objects occur in successive images (e.g., Vila et al., 2008). The overlapping method is feasible by using a 5-min satellite image timestep.

To define the boundaries of individual cloud objects, the cloud tracking method uses 10.35 μm BTs that are sensitive to cloud particles (their size, phase, and amount) in the upper portion of the cloud, which helps separate cloud clusters through time. Fiolleau and Roca (2013) describe the cloud detection as iteratively growing cloud "seeds" from colder to warmer BTs. Cloud objects are identified by detecting initial boundaries using a low BT threshold of 210K. For each identified object, pixels are added to the cold cloud-top object using a 2.5K warmer BT threshold to identify the edge of the new boundary. The warmer BT threshold is also applied to detect new cloud objects at warmer BTs up to 285K.

Cloud objects reaching CI are tracked over time and are defined as when a cloud object in the 10.35 μm BTs contains a radar reflectivity of 35 dBZ or higher within its cloud boundary (e.g., Henderson et al., 2021; Mecikalski & Bedka, 2006; Weckwerth & Parsons, 2006). Ground-based reflectivities from level 2 NEXRAD weather radars are matched to the individual cloud objects. When the radar reflectivity within a cloud object surpasses the 35 dBZ threshold, that time step is labeled time lag 0 and the data before, during, and after this CI time step are composited to describe the evolution of the cloud objects. The same radar-based reflectivity CI threshold is applied to the simulation experiments. In WRF, the Thompson microphysics scheme computes the output of a radar reflectivity factor based on the Rayleigh approximation, which is very similar to the S-band wavelength observations of the ground-based radar data (e.g., Li et al., 2022). As in Henderson et al. (2021), tracking of observed and simulated cloud objects focuses on objects whose BTs grow colder than 250K at some point in their evolution. For brevity, the term "CI clouds" will refer to clouds reaching 250K during their lifecycle indicating a cloud that is likely to produce heavy precipitation. Therefore, the analysis concentrates on clouds that grow into heavily precipitating clouds and helps remove possible biases from the overproduction of cloud objects in the NWP simulations (e.g., Davis et al., 2009; Griffin et al., 2017; Henderson et al., 2021). The advantage of comparing tracked CI objects over time is that it allows the evaluation to focus on the model's ability to simulate the evolution of convection independent of the cloud location and time. The evaluation can then be applied to gain greater understanding of the physical processes occurring within the clouds that lead to various cloud-top signatures depicted in satellite IR imagery and each WRF simulation.

3. Results

This analysis first examines differences in cloud top evolution in the simulations and compares them to the observed BTs to determine which LSM provides a more realistic depiction of the cloud evolution. Differences in the surface energy budget and their environmental impacts are then discussed to better understand why the cloud evolutions differ. Finally, the model data is used to evaluate how environmental differences due to the change in LSM lead to physical changes in cloud properties and structure.

3.1. Evolution of Cloud Top Brightness Temperatures

The effect of the LSM can be examined by investigating changes in cloud top BT growth between the WRF experiments and observations. Cloud BT comparisons are first assessed from a domain-wide point of view. To illustrate differences between the two LSM experiments, the number of CI cases over the 3-hr period (1700–2000 UTC) and their cloud object areas are shown in Figure 2. Overall, it is evident that there are large differences between the simulations. The Noah-MP and Noah LSMs produce a higher occurrence of CI clouds compared to the GOES-16 observations, mainly between 1830 and 1930 UTC. Henderson et al. (2021) found that this overestimation was related to an overproduction of clouds with BTs remaining warmer than 250K. Near 1845 UTC, the number of CI clouds in both simulated and observed cases begins to plateau or decrease (Figure 2a). While the number of CI cloud objects is similar toward the end of the experiments, the cloud objects using the Noah-MP LSM are larger (Figure 2b), which better matches the observed cloud-top areas from the GOES-16 ABI. Along with the smaller clouds from the Noah experiment, the Noah LSM leads to a distinct delay in CI

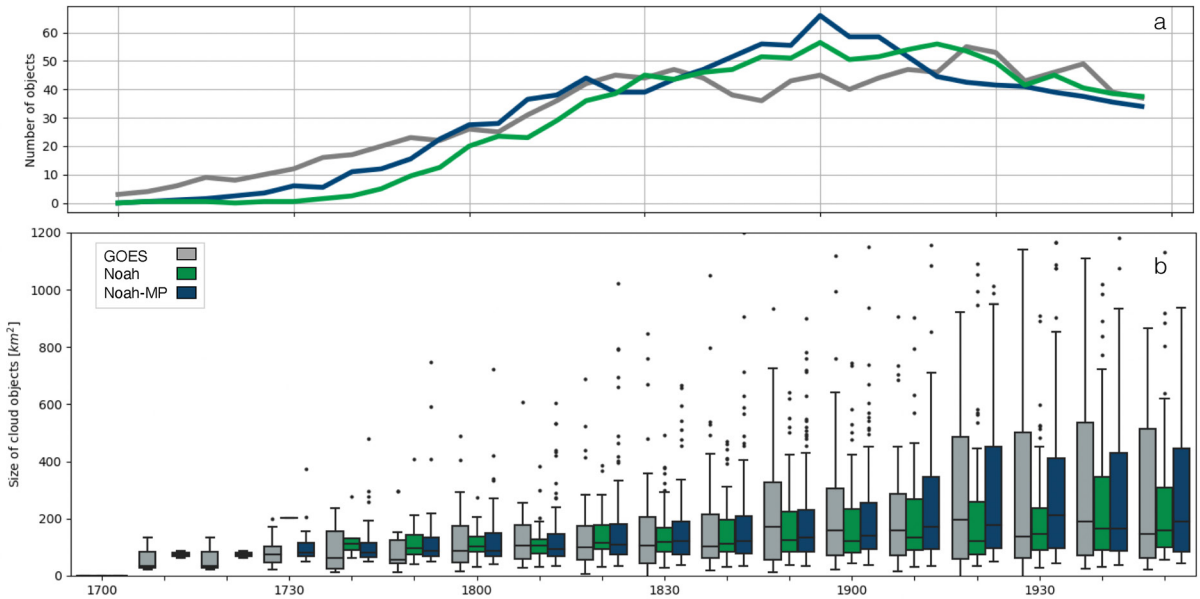

Figure 2. The evolution of convective initiation (CI) occurrence and cloud top extent from 1700 to 2000 UTC. The (a) occurrence of active CI cloud objects containing a reflectivity higher than 35 dBZ at each time step and (b) the distribution of CI cloud objects sizes for GOES-16 (gray) observations and Noah-MP land surface model (LSM) (blue), and Noah LSM (green) Weather Research and Forecasting experiments shown using box-and-whisker diagrams.

formation (Figure 2a) before 1800 UTC compared to the Noah-MP LSM and GOES-16 observations. The differences in cloud size are apparent in BT snapshots for two times during the WRF experiments (Figure 3). At 1800 UTC (Figures 3a–3c), CI clouds in the Noah-MP experiment begin to develop most prominently over the northeast quadrant of the domain, which primarily contains forests and croplands. The difference in cloud-top extent

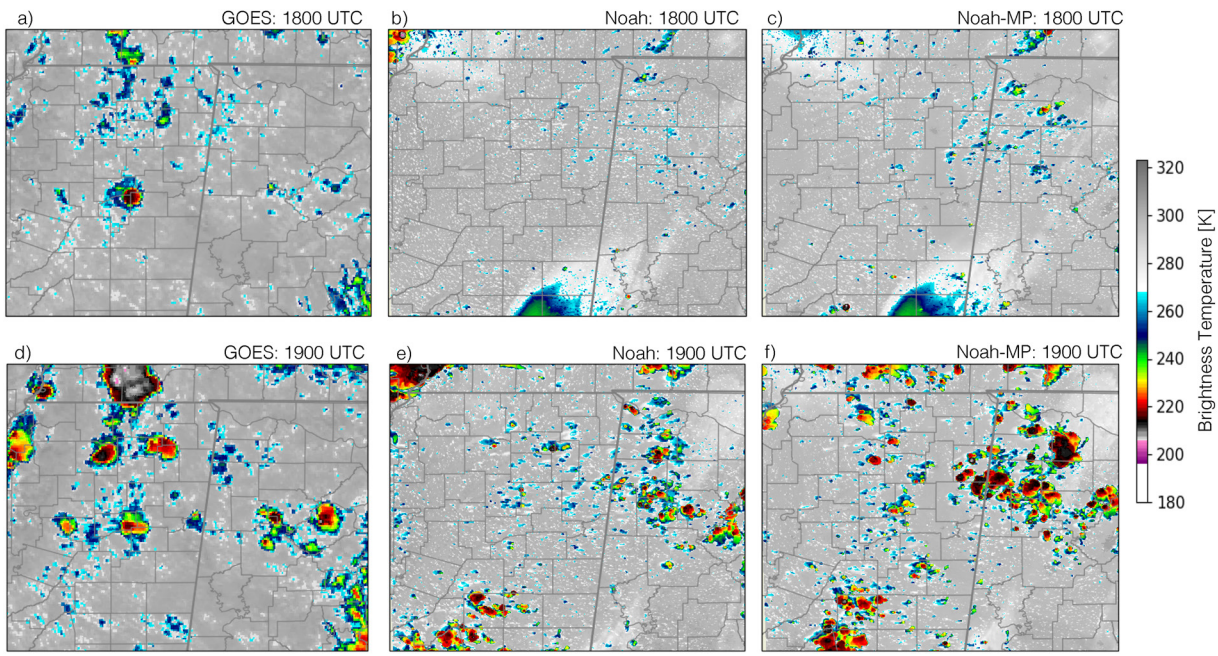

Figure 3. Comparison of the observed and simulated Advanced Baseline Imager 10.35 μm brightness temperatures (K). Brightness temperatures (BTs) at 1800 UTC for (a) GOES-16, (b) the Noah land surface model (LSM), and (c) Noah-MP LSM, respectively. BTs at 1900 UTC for (d) GOES-16, (e) the Noah LSM, and (f) Noah-MP LSM, respectively.

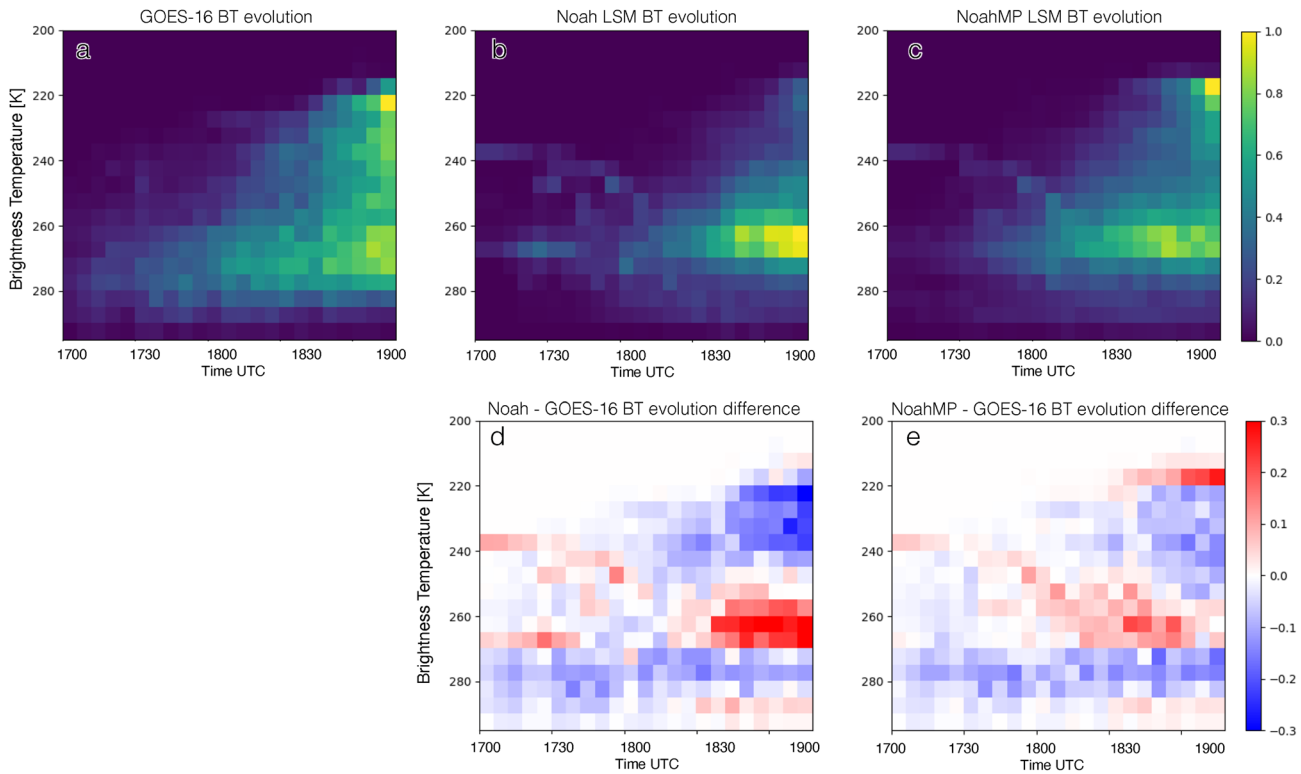

Figure 4. 2D-histograms of normalized Advanced Baseline Imager 10.35 μm brightness temperature occurrence from 1700 to 1900 UTC for (a) GOES-16, (b) Noah land surface model (LSM), and (c) Noah-MP LSM. The difference in normalized occurrences between GOES-16 and the Weather Research and Forecasting experiments are shown in (d) for the Noah LSM and (e) for the Noah-MP LSM.

becomes more apparent at 1900 UTC (Figures 3d–3f), particularly in the northeast quadrant, where the coverage of high cloud tops (i.e., BTs <250K) is larger in the Noah-MP experiment.

To examine the differences in the cloud top characteristics, Figures 4a–4c show the evolution of the BTs at 5-min intervals for all CI clouds tracked during their entire lifecycle for the observations and each model experiment. To more easily assess differences between the observed and simulated 10.35 μm BT distributions, each 2D histogram is normalized and differenced (Figures 4d and 4e). Early in the time period, there is a distinct BT signature in the simulations near 240K related to a cloud shield in the southern portion of the domain that moves out of the domain by 1800 UTC (Figures 3b and 3c). In Figure 4, the observed and simulated histograms contain BTs of warmer cloud tops ranging between 260 and 275K throughout the time period. The observations, however, contain more frequent BTs of warm cloud tops near 275K. After 1800 UTC, a higher occurrence of BTs colder than 240K begins to appear. This is most prominent in the observed BTs and Noah-MP LSM BTs. Beyond 1830 UTC, the WRF experiments contain a bimodal peak of BTs near 260 and 220K. The GOES-16 observations contain a broader distribution of BTs compared to the bimodal cloud distributions from the models. The difference fields (Figures 4d and 4e) show that the model simulations overpredict clouds near 260K. This increase in mid-level convection is amplified with the Noah LSM, whereas the Noah-MP LSM produces a more accurate distribution of higher cloud tops—albeit producing more frequent upper-level clouds at BTs <220K. The delay in cloud growth is evident for Noah LSM (Figure 4d) with a lower frequency of cloud top BTs <240K after 1800 UTC.

To investigate temporal biases in cloud evolution, Figure 5 shows the distribution of cloud top BTs as a function of time from 30 min before until 30 min after CI detection. Both of the LSM experiments contain a similar cooling of cloud top temperatures before the time of CI. For the model simulations and observed ABI BTs, the cloud growth (i.e., cloud top getting colder) is slower during the 30 min before CI is detected. A jump toward colder BTs at the cloud top occurs near CI detection, where the models and observations exhibit accelerated cloud growth once CI occurs. Henderson et al. (2021) demonstrated that this jump in growth is associated with an increase of in-cloud ice content that produces the latent heating necessary to sustain cloud development. The main difference

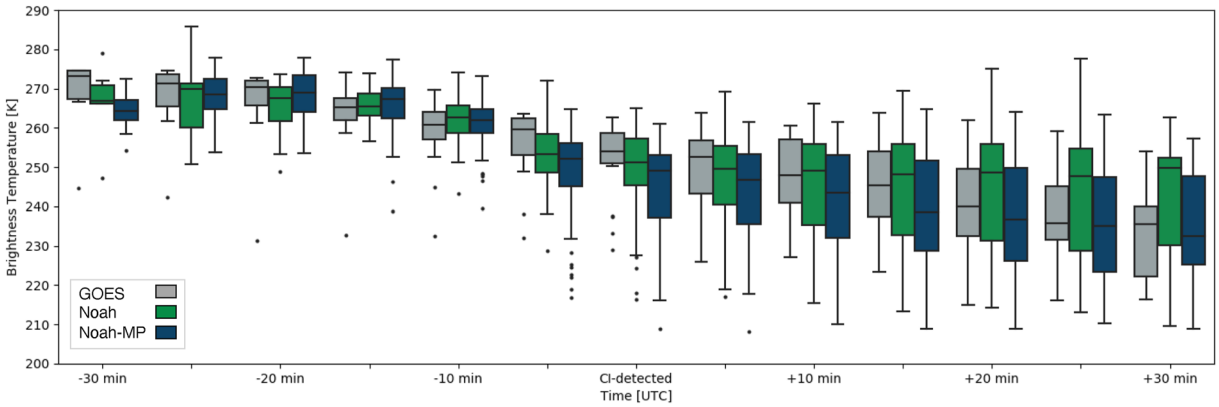

Figure 5. Box-and-whisker plots of Advanced Baseline Imager 10.35 μm brightness temperatures (K) for GOES-16 (gray), Noah land surface model (LSM) (green), and Noah-MP LSM (blue). Bars are spaced at 5-min intervals of 30 min before and after convective initiation (CI) was detected. Time = 0 is defined as the time CI was detected.

between the model experiments occurs around 15 min after CI, where the Noah clouds exhibit a reduction or a cessation of in-cloud growth. The Noah-MP BTs, however, continue to cool, which suggests that CI clouds from the Noah-MP experiment develop into deeper convection at a rate more similar to that observed by the GOES-16 ABI. Within this analysis, the Noah-MP LSM provides a better representation of the spatial extent of CI clouds and convective growth.

3.2. Evaluating the Surface Energy Budget

Isolated convective clouds and precipitation are more common over the heterogeneous vegetation in the Southeastern United States compared to other regions such as the Great Plains (Gambill & Mecikalski, 2011; Kirshbaum et al., 2016; Miller & Mote, 2017; Rickenbach et al., 2020). Varying assumptions between LSMs can lead to large differences in the surface energy balance between adjacent land cover types and thus influence the development of mesoscale circulations responsible for aiding convective development (e.g., Avissar & Pielke, 1991; Weaver, 2004). Changes in the circulation could explain the cloud top extent differences illustrated in Figure 2. To diagnose potential reasons for cloud top BT and extent differences, the downward and upward shortwave (SW) and longwave (LW) emissions, along with the latent heat (LH) and sensible heat (SH) fluxes at the surface are examined for the first 2 hr of the analysis period (1700–1900 UTC). The surface energy balance comparison focuses on a subset region in the eastern half of the domain (dashed box in Figure 1b) that contained larger differences in cloud extent (Figures 2 and 3). This region is comprised of mostly forested vegetation mixed with grassland/cropland. Each energy budget component is compared for all-sky conditions starting right before CI is detected in the model and GOES-16 observations until when the subset region begins to fill with high clouds.

Comparing the surface energy components across the region sheds light on the differences in the land-atmosphere interactions occurring in each model experiment. In Figure 6, it is evident that LH in the Noah experiment is consistently higher than Noah-MP by ~45 W m^{-2}. This difference is initially balanced by the Noah-MP via increased SH at the beginning of the analysis period; however, the SH becomes more similar later in each experiment as cloud sizes grow and precipitation increases. In Figures 6a and 6c, LH and SH comparisons are also shown for clear-sky conditions. For Noah-MP, the SH does not drop off as quickly in clear-sky conditions. Figures 6b and 6d illustrate that the differences are generally consistent over the model domain where the LH and SH discrepancies related to vegetation are apparent between the grassland/cropland and forested regions. The land-based comparisons are split into conditional means of two land-based categories for any land types containing grasslands or cropland and land-based categories for all forested land types. The conditional mean LH and SH for the forests agrees with the overall domain-wide results, but the opposite signal occurs over cropland/grassland regions. For the Noah-MP LSM, regions with grassland/cropland types have lower sensible heat conductance. Further, the grassland/cropland regions are characterized by higher evaporation rates in comparison to transpiration rates, which is due to lower vegetation fractions along with a lower leaf area index. These factors ultimately lead to higher LH and lower SH in the grassland/cropland regions compared to forested regions. The LH and SH

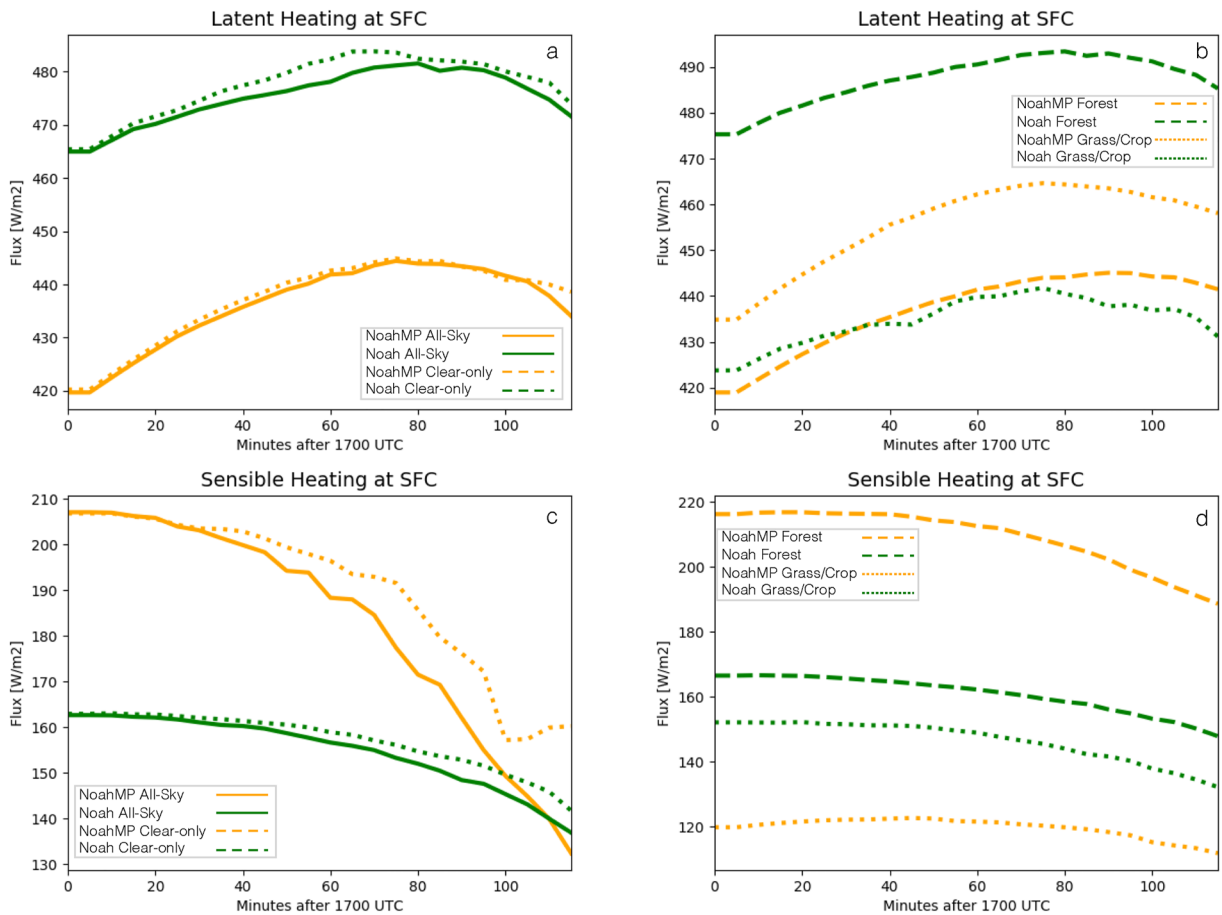

Figure 6. 5-min (a) surface latent heat flux for clear (dashed lines) and all-sky (solid lines) conditions and (b) surface latent heat flux split into conditional means of land types containing grasslands or cropland and land-based categories for all forested land types, (c) surface sensible heat flux for clear and all-sky conditions, and (d) surface sensible heat flux split into conditional means of land types containing grasslands or cropland and land-based categories for all forested land types. All units are W m^{-2} and provided over a 2-hr period starting at 1700 UTC.

differences are generally consistent over the model domain (Figure 7), where the LH and SH discrepancies are related to differences in vegetation. The largest differences are apparent between the grassland/cropland regions (Figure 1b). This is qualitatively illustrated by regions of negative SH differences in Figure 7f for grassland/cropland regions and positive SH differences in Figure 7f over the forested regions.

The means of all surface energy components from 1700 to 1800 UTC are shown in Table 1. The largest differences occur in the upward fluxes from the surface to the atmosphere. Consistent with the time series in Figure 6, the SH and LH fluxes are +46 and –43 W m^{-2}, respectively, with higher SH (lower LH) in the Noah-MP experiment. The SH and LH discrepancies could be related to the canopy representation in forested land types from the Noah-MP LSM. The Noah-MP surface albedo is systematically lower across the model domain (Table 1), with differences being largest over the forested regions (Figure 8). In particular, the mixed forest region land types contain albedo differences of around 5%. Greater surface absorption is apparent by the decreased upwelling SW radiation as well as the increased ground heat flux (heat storage) shown in Table 1. As evidenced by the larger ground heat flux in the Noah-MP experiment, differences in albedo as well as the assumed thermal emissivity characteristics for the vegetation types also lead to a radiative imbalance at the surface. The reduced upwelling LW radiation and LH (evaporative cooling) in Noah-MP are due to greater land surface heat storage, which would then be released to heat the atmosphere at later model timesteps.

To investigate the different impacts of LH and SH on the atmosphere, the evolution of simulated relative humidity and air temperature on the model is shown in Figure 9. The difference in the air temperature demonstrates that the ambient air is warmer and drier within the PBL in the Noah-MP experiment (Figure 9a) before 1730

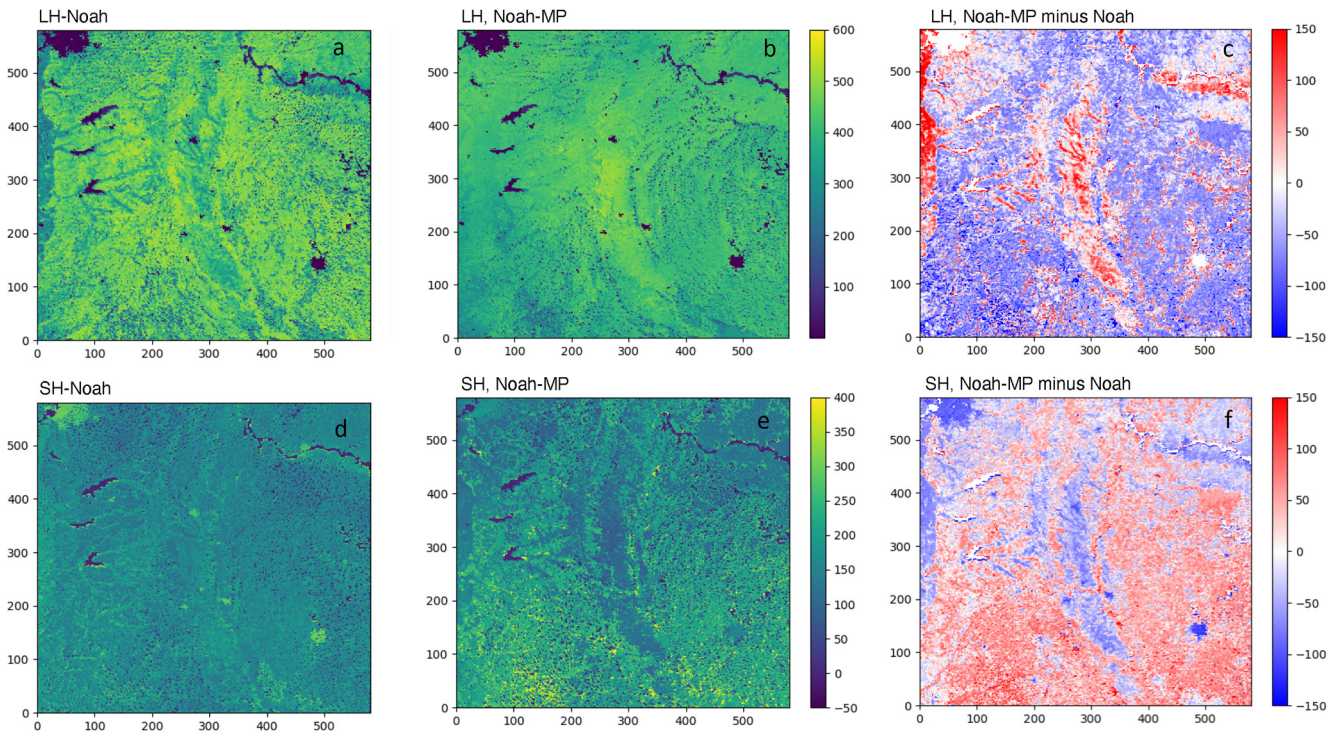

Figure 7. Surface latent heat flux (W m^{-2}) over the domain for (a) Noah land surface model (LSM) and (b) the Noah-MP LSM. Surface sensible heat flux (W m^{-2}) for (c) the difference between Noah LSM and Noah-MP LSM latent heating. Surface latent heat flux (W m^{-2}) over the domain for (d) the Noah LSM, (e) the Noah-MP LSM, and (f) the difference between Noah LSM and Noah-MP LSM sensible heating. Flux values are taken at 1700 UTC before convective initiation was observed in the experiments.

UTC. This is consistent with the differences in the surface energy balance from Figure 7 as higher SH will act to warm the lower atmospheric layers. While the surface and boundary layer are initially drier in the Noah-MP experiment, a slight but potentially important increase in the PBL height can be seen in Figure 9b. For both experiments, the PBL is near 1.5 km AGL, but the PBL in the Noah LSM is around 100–200 m deeper. This slight difference in PBL height is indicated by the band of lower relative humidity near the top of the PBL, which could impact cloud inflow and updraft characteristics (Murzdek et al., 2022). While the surface and boundary layers are drier in the Noah-MP experiment, the relative humidity increases in the upper-troposphere after 1800 UTC in Noah-MP. Similar results in clear-sky conditional relative humidity means (not shown) are found when compared to the all-sky in Figure 9b. Higher relative humidity in the upper-troposphere could provide an environment more favorable for upper-level cloud growth (e.g., Henderson et al., 2018). Dai et al. (2021) describe that regions with higher LH flux could preferentially trigger convection by lowering the level of free convection (LFC) closer to the top of the PBL. While both the Noah and Noah-MP experiments contain high LH values, the increased SH in Noah-MP will aid in providing the buoyancy needed to reach the LFC and, therefore, the Noah-MP LSM would be more likely to trigger and sustain deep convection.

Table 1
Domain and Time Averaged Values for Individual Components of the Surface Radiation Budget for Each of the Model Experiments

	Noah-MP	Noah	Difference (NoahMP-Noah)
$SW_{D,sfc}$	988	992	−4
$LW_{D,sfc}$	405	406	−1
$SW_{U,sfc}$	133	168	−35
$LW_{U,sfc}$	493	521	−28
SH_{sfc}	208	162	+46
LH_{sfc}	420	463	−43
Ground flux	133	75	+58
Sfc emissivity	0.99	0.95	+0.04
Sfc albedo	0.14	0.17	−0.03

Note. Included elements in the table are: downwelling SW ($SW_{D,sfc}$), downwelling LW ($LW_{D,sfc}$), upwelling SW ($SW_{U,sfc}$), upwelling LW ($LW_{U,sfc}$), surface sensible heat flux (SH_{sfc}), surface latent heat flux (SH_{sfc}), ground heat flux, surface emissivity, and surface albedo. All units are in W m^{-2} with the exception of albedo and emissivity which are unitless.

Previous research has demonstrated that differences in the surface energy balance are likely to lead to changes in the local mesoscale circulation (e.g., Anthes, 1984; Duda et al., 2017; Pielke, 2001; Santanello et al., 2018). Figure 10 illustrates low-level divergence (950 hPa) and maximum vertical velocity over the entire column at a given grid point between the two simulations. Blue colors in Figures 10a and 10b show where the LSM experiments

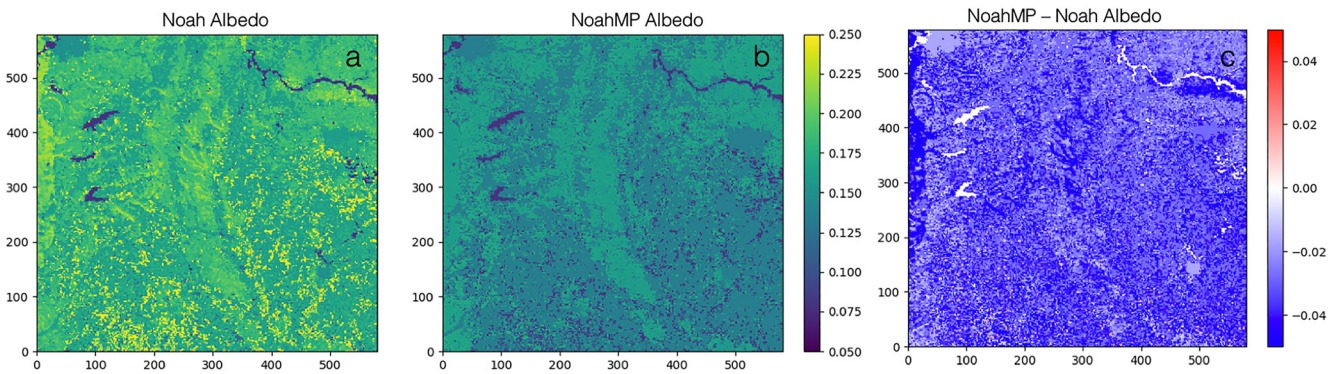

Figure 8. Surface albedo across the domain for (a) Noah land surface model (LSM) and (b) the Noah-MP LSM, and (c) the difference between Noah and Noah-MP. Albedo values are taken at 1600 UTC.

contain increased surface convergence (i.e., negative divergence) and more yellow colors in Figures 10c and 10d are regions where this experiment has higher maximum vertical velocities. The higher vertical velocities for both LSM experiments are most noticeable in the northeast section of the model domain containing pockets of forests, grassland, or cropland. Regions of stronger near-surface convergence and vertical velocities occur within forested land types. This is particularly prominent near the boundaries of forested and grassland/cropland regions. The higher velocities are more noticeable in the Noah-MP LSM experiment. These conditions are supported by high afternoon convective available potential energy, which provides a more ideal region for cloud formation. Figure 11 illustrates that high convective available potential energy (CAPE) ≥1500 J kg^{-1} is ubiquitous in the model domain. Further, Figures 11c and 11d illustrate that the LFC is near 1.5–2 km for both experiments. The low LFC is close to the top of the PBL (1.5 km) and provides evidence of an environment preferential to triggering convection.

To more clearly illustrate this relationship, Figure 12 compares the low-level divergence (950 hPa) against the maximum vertical velocities. The scatterplots in Figures 12a and 12c utilize all land types, whereas the scatterplots in Figures 12b and 12d are separated into two land-based categories; colors in blue are for any land types containing grasslands or cropland and colors in black are for all forested land types. In general, both LSM experiments exhibit a trend that as the surface convergence increases, it corresponds with higher maximum vertical velocities. The Noah-MP LSM produces regions with higher convergence near the surface along with stronger vertical velocities, especially where a forested vegetation type is prominent (Figure 12d). Further, the Noah-MP LSM has a larger contrast in the strength of convergence between the forested and grassland/cropland regions compared to the Noah LSM. This signal agrees with the larger regional differences in SH shown in Figure 7.

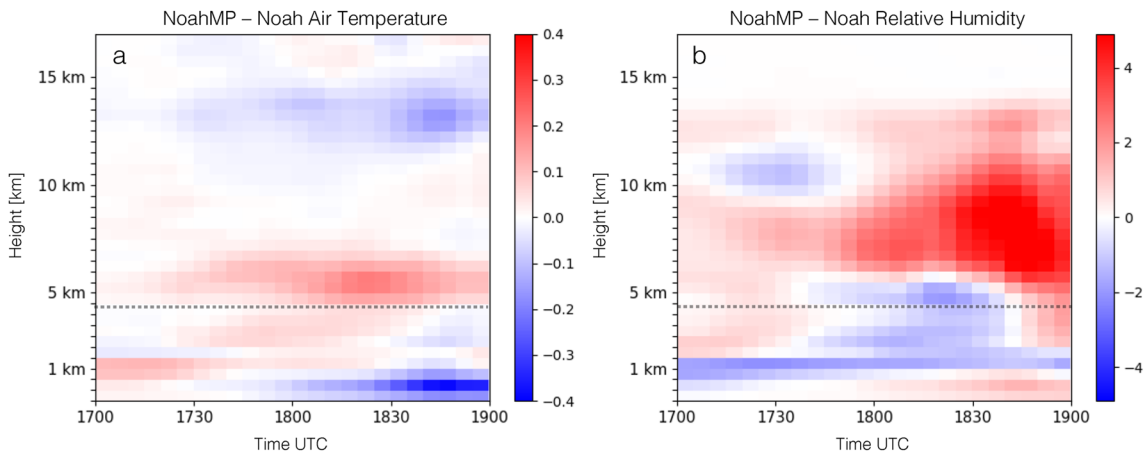

Figure 9. Differences in (a) ambient air temperature and (b) relative humidity between the model experiments. Differences are defined as Noah-MP land surface model (LSM) minus Noah LSM values. Values are displayed as a domain average across the subset region at each vertical sigma layer. The dashed line references the domain averaged freezing level.

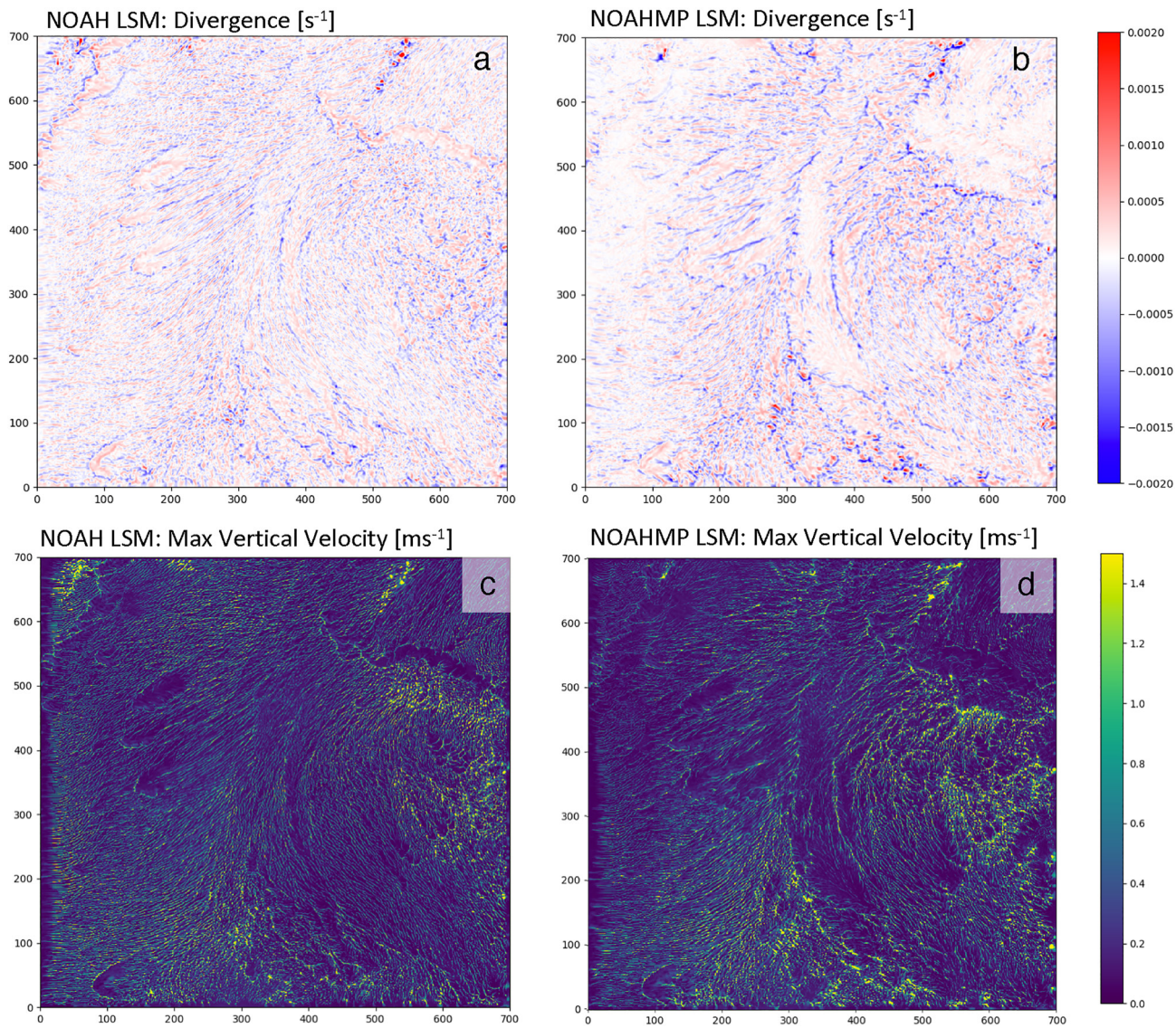

Figure 10. Maximum vertical velocity in the column at each model grid point for (a) Noah land surface model (LSM) and (b) the Noah-MP LSM and near-surface divergence at 950 mb for (c) Noah LSM and (d) the Noah-MP LSM. Values are taken at 1700 UTC before convective initiation was observed in the experiments.

3.3. Physical Impacts on Convective Updrafts and Cloud Properties

This section examines the differences in vertical profiles of updrafts and cloud properties between model experiments. Updraft characteristics are evaluated using methods similar to Morrison et al. (2012) and Lebo and Morrison (2015) who derived the profiles of vertical mass flux and updraft fraction from WRF simulations. For this work, the vertical convective mass flux (Equation 1) is defined at each vertical sigma level using the vertical velocity, w, and the air density, ρ, for all locations with a CI cloud object containing $w \geq 2$ m s^{-1}. The updraft fraction (Equation 2) is defined as the fraction of the convective updraft ($w \geq 2$ m s^{-1}) compared to the area of all regions of updraft in a cloud object. The resulting updraft mass flux and updraft fraction at the sigma levels are then averaged at 500 m increments from the surface to 12 km.

$$\text{Mass Flux} = \frac{w\,\rho}{\text{Cloud Area}} \tag{1}$$

$$\text{Updraft Fraction} = \frac{\text{Cloud Area}, w \geq 2\text{ms}^{-1}}{\text{Cloud Area}, w \geq 0\text{ms}^{-1}} \tag{2}$$

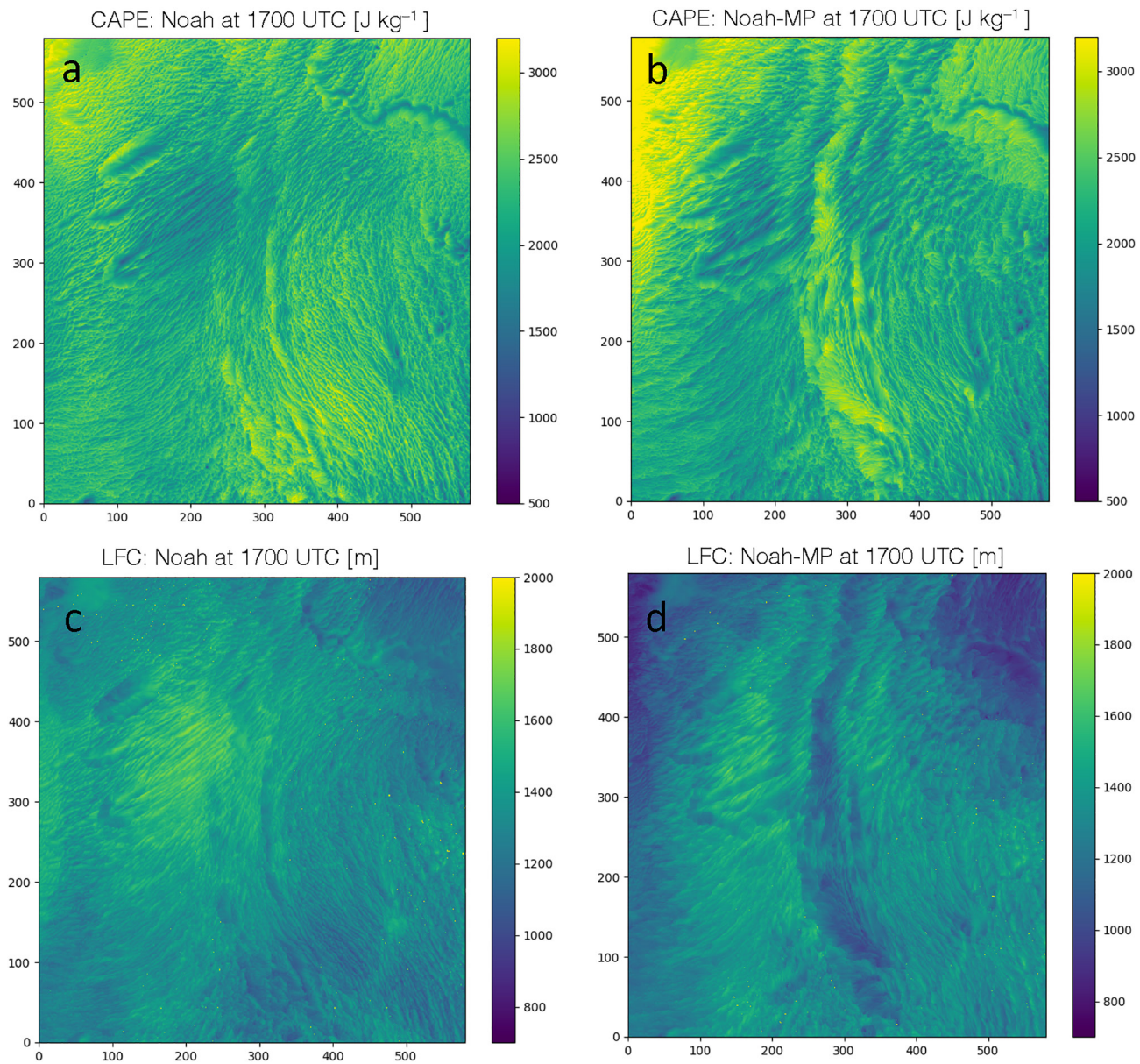

Figure 11. Convective available potential energy [J kg^{-1}] for (a) the Noah land surface model (LSM), (b) the Noah-MP LSM. The level of free convection [m] for (a) the Noah LSM and (b) the Noah-MP LSM. Values are derived at 1700 UTC.

Figure 13 displays the vertical profiles of updraft mass flux (Figures 13a–13c) and updraft fraction (Figures 13c–13f). For each variable, the panels show the evolution of mass flux and updraft fraction starting 15 min before CI is detected, the time of CI detection, and 15 min after CI was detected. To help confirm that the differences in the mass flux and updraft fraction are not related to temporal differences (e.g., the delay in CI for Noah LSM in Figure 2), we have included two different time periods. The solid lines display results for all time periods, whereas the dashed lines display results for CI detected only after 1800 UTC. Both time periods yield similar results; therefore, the resulting discussion will focus on the solid lines in Figure 13. For the updraft mass flux 15 min before the detection of CI (Figure 13a), there is little difference in the amount of mass moved upward through the updraft. This agrees with Figure 5, where the general growth pattern of the cloud-top temperatures and extent are similar between the model experiments and GOES ABI. At the time of CI (Figure 13b), the Noah-MP experiment (orange line) has a greater average cloud object updraft mass flux starting at 3 km that persists to the upper portions of the cloud above 10 km. The increased mass flux in Noah-MP continues 15 min

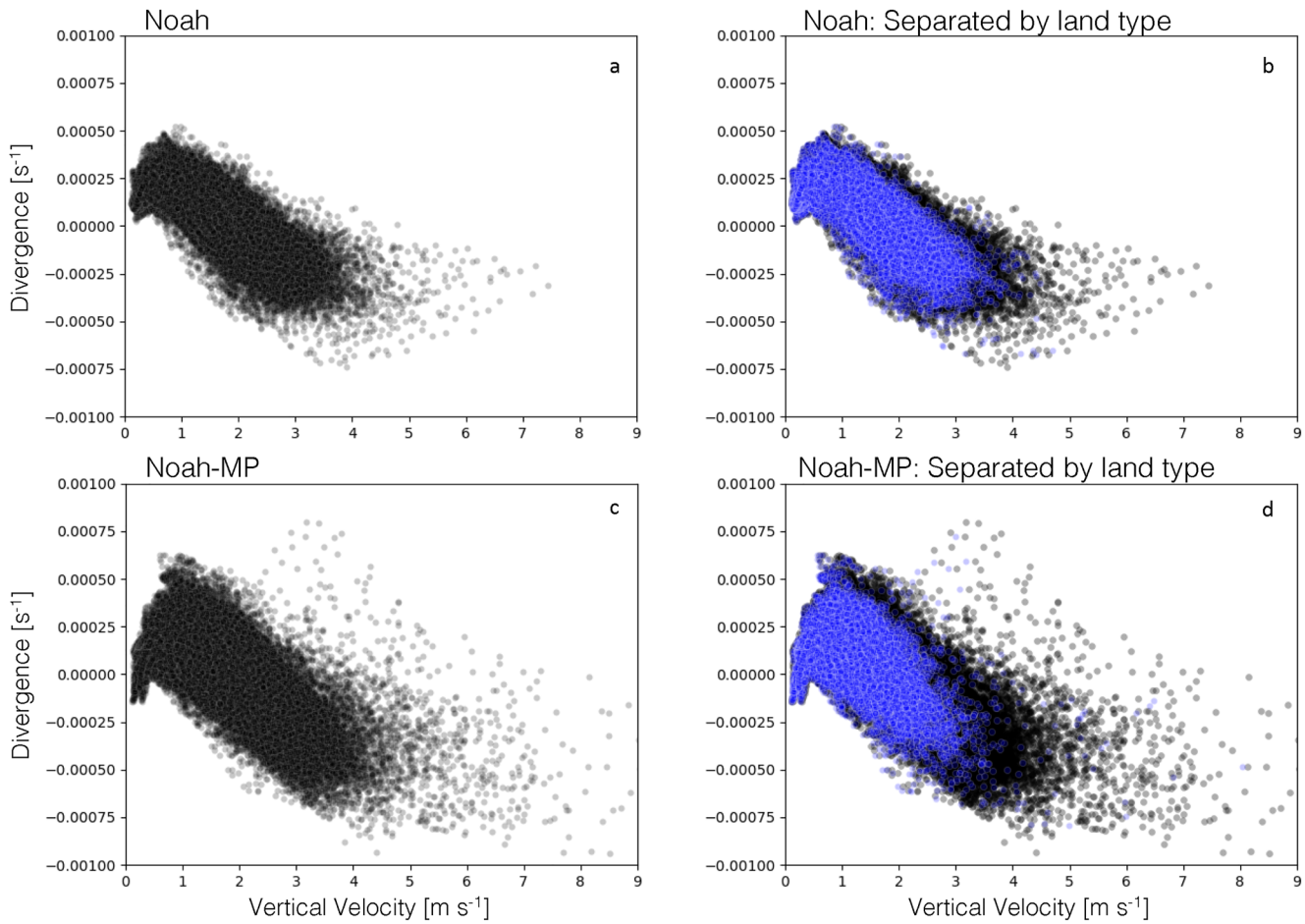

Figure 12. The relationship between the maximum vertical velocity in the column at each grid point near surface divergence at 950 mb. Panels are shown for (a) Noah land surface model (LSM), (b) Noah LSM split into forested or non-forested land types, (c) Noah-MP LSM, and (d) Noah-MP LSM split into forested or non-forested land types.

after CI detection (Figure 13c) with a slight increase of mass flux above 5 km, which is above the freezing level (near 4 km). CI clouds in the Noah-MP experiment contain stronger updrafts and flux more water above the freezing level after CI is detected.

The increased updraft mass flux is consistent with differences in updraft fraction between the two experiments (Figures 13d–13f). Convective updraft size is larger in Noah-MP near 4 km 15 min before CI; however, 15 min after CI, the larger fraction of convective updrafts in Noah-MP is focused in the upper levels of the cloud. This indicates that larger/stronger updrafts reach higher into the clouds after CI detection. This implication is consistent with the cloud growth after CI in Figure 5, where the Noah-MP and observed clouds sustain growth beyond 15 min of CI detection, while cloud growth appears to stall in the Noah experiment. A snapshot of updraft velocities shows the distribution of vertical velocities ($w \geq 0.1$ ms^{-1}) for CI clouds (Figure 14). The median values (black lines in boxes) are similar for each model experiment between 4 and 8 km; however, the Noah-MP experiment contains more cloud objects in the high portions of the whisker and outlier distribution. From 8 to 11 km, the Noah-MP vertical velocities are consistently skewed higher. This agrees with the resultant mass flux and updraft fraction differences in Figures 13c and 13f.

Past observational work has indicated that the accelerated and sustained growth of deep convection after CI is related to an increase in ice formation within the upper levels of the cloud (Henderson et al., 2021; Mecikalski et al., 2016; Senf & Deneke, 2017; Zipser, 2003). The differences in cloud top evolution shown in Section 3.1 could be related to differences in water content fluxed from the lower levels of the cloud to above the freezing level. Increased moisture flux to upper levels would lead to increased ice formation, in-cloud latent heating, and

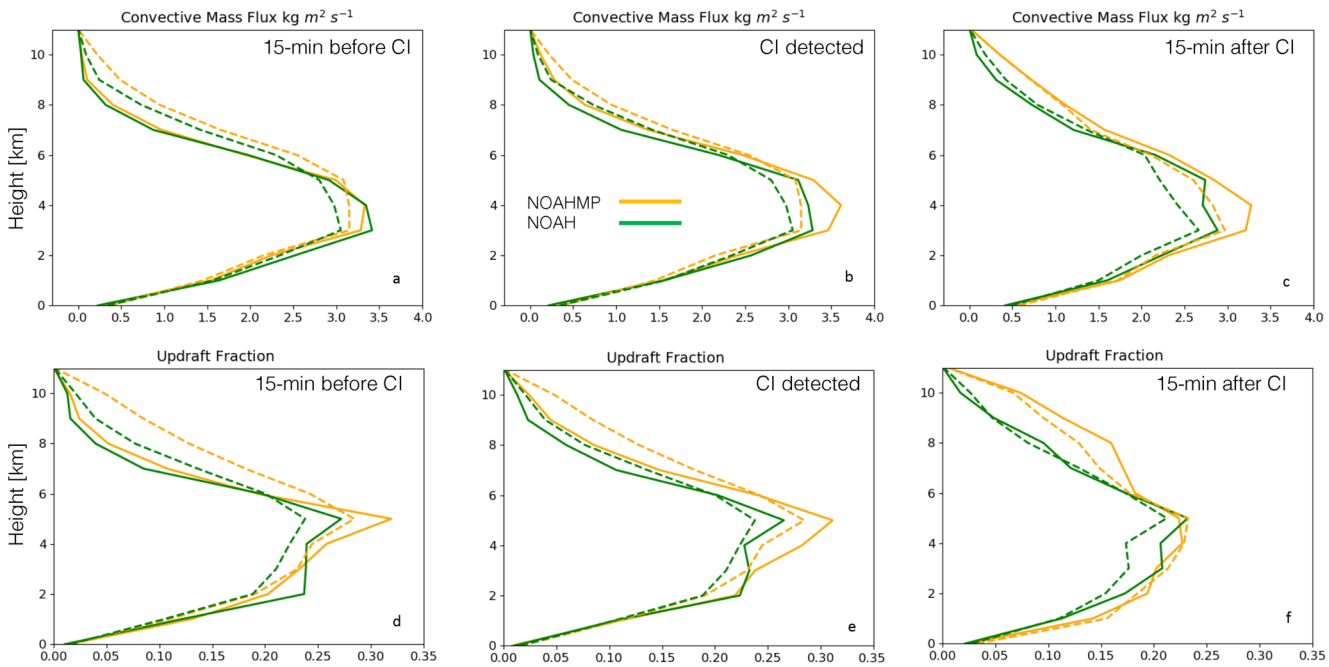

Figure 13. Evolution of mean profiles for (top) convective mass flux and (bottom) updraft fraction from 15 min before convective initiation (CI) until 15 min after CI was identified. Dashed lines indicate results isolated only to CI detected after 1800 UTC.

therefore cloud growth. By comparing simulated clouds that best matched GOES ABI growth rates, Henderson et al. (2021) demonstrated that CI cloud growth from multiple microphysics schemes was proportional to the ice formation at cloud top. Clouds that do not advect enough cloud water from the lower levels to the upper levels could not sustain growth. Figure 15 shows the differences in cloud hydrometeor mixing ratio profiles for CI detected clouds from 1700 to 1900 UTC, where red colors show when the Noah-MP simulation contains higher mixing ratios in the cloud. In Figure 15a, the Noah-MP liquid cloud mixing ratios are consistently higher above

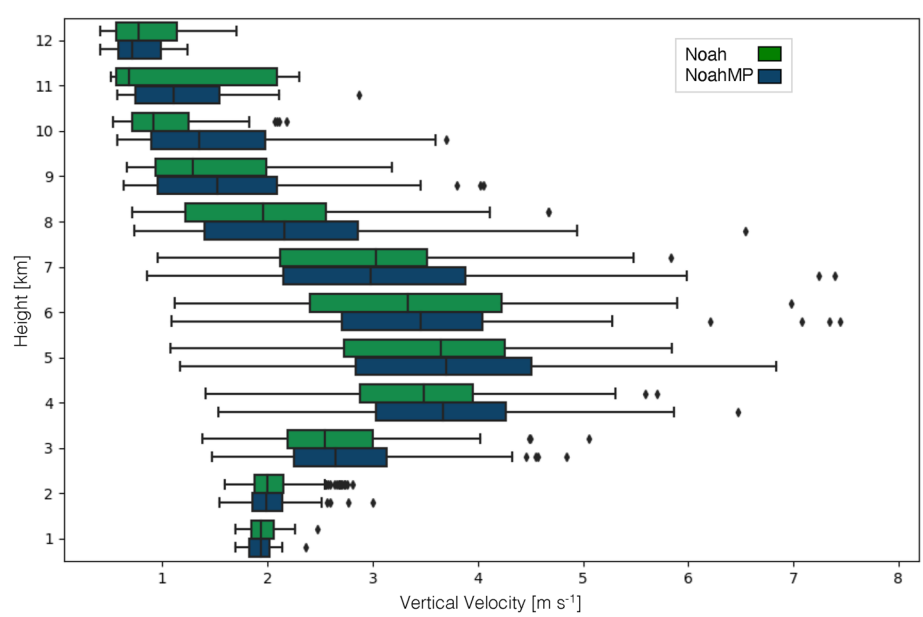

Figure 14. Weather Research and Forecasting model simulated updrafts ($w > 0.1$ m s^{-1}) for the Noah and Noah-MP land surface models (LSMs). Values are derived for cloud objects 15-min after convective initiation was detected. Data are presented in a box-and-whiskers format and all values have been averaged over 1-km layers.

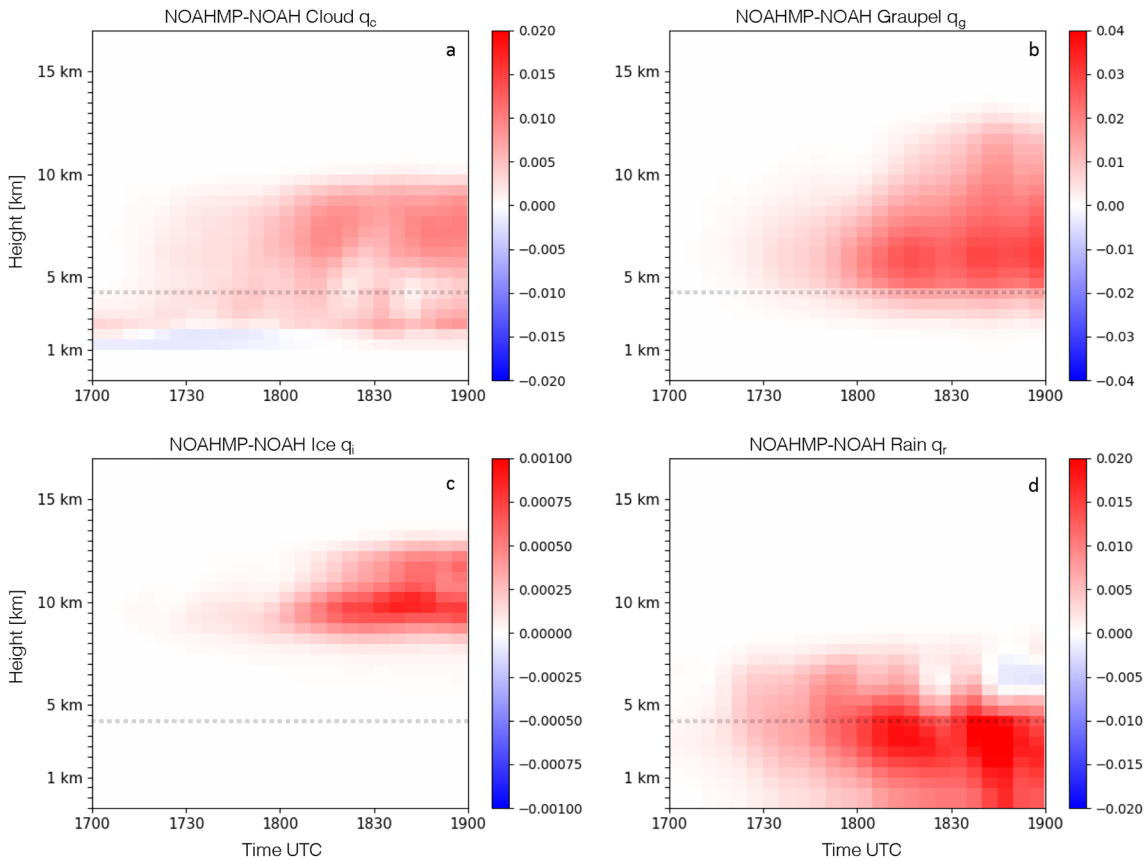

Figure 15. Domain-wide differences in simulated cloud mixing ratios for (a) cloud water (q_c), (b) graupel (q_g), (c) cloud ice (q_i), and (d) cloud rain water (q_r). Differences are defined as Noah-MP land surface model (LSM) minus Noah LSM values over a 2-hr period starting at 1700 UTC. The dashed line references the domain averaged freezing level.

the PBL (~1.5 km) and the higher cloud water contents monotonically increase into the upper levels. The higher mass flux in the convective clouds results in more cloud water and thus more graupel and ice formation in the upper levels (Figures 15b and 15c). With more graupel in the upper levels of the cloud and continued cloud growth, the resulting clouds also contain higher rainwater content above the freezing level (Figure 15d), which eventually leads to more rain at the surface. Henderson et al. (2021) demonstrated that increased rain content was consistent with sustained cloud growth.

4. Summary and Discussion

In this study, we described the impacts of LSMs on simulated convection and its cloud evolution. These sections showed that: (a) the Noah LSM and Noah-MP LSM can have substantially different impacts on the size and growth of convection after the cloud reaches CI. By comparing the simulated cloud evolution to the GOES-16 ABI observations, the Noah-MP LSM provides a more representative cloud top size distribution and growth rate of convection. (b) The changes in convective growth are largely related to the partitioning between surface SH and LH fluxes. The higher SH from Noah-MP LSM results in enhanced local forcing over forested regions. Increased surface convergence was largest near the boundaries of cropland and forested areas, which resulted in higher peak vertical velocities within those transition regions. (c) The strongest low-level convergence and upward vertical velocities occurred in the Noah-MP experiment. This was related to CI clouds with higher convective mass flux, which led to more cloud water advected higher in the troposphere and greater upper-level ice content.

The use of GOES-16 ABI IR data helped examine the accuracy of cloud-top growth for CI clouds that reach 250K cloud-top temperatures at some point during their lifecycle. Comparing only CI clouds demonstrates that the growth of convection is quite sensitive to the LSM. As the model simulations progress in this case study, the

cloud extent from the Noah-MP experiment begins to exceed the Noah experiment around 1800 UTC. Comparison to the satellite observations showed that the larger growth from Noah-MP more closely matches reality. Overall, larger cold cloud tops were found in both simulations over the forested region in the northeast portion of the domain, whereas the observed ABI clouds exhibit large growth across the entirety of the northern portion of the domain.

The largest growth for both the observed and simulated clouds occur in regions containing forested vegetation types. In the Noah-MP LSM, the albedo is lower in the domain, especially in forested regions compared to the Noah LSM, which increased surface absorption of solar radiation, SH, and ground heat flux. Sensitivity analyses within the experiments demonstrated that forested land was necessary to produce the longer-lived storms. When testing Noah-MP sensitivity experiments, if the forested land was removed or the green vegetation fraction was reduced below 50%, CI was significantly suppressed. The representation of the forested canopy and its green fraction are important factors in aiding CI and sustainment of convection. Increased SH in the forested regions provides an additional forcing in the Noah-MP experiment that helps grow convection by inducing stronger surface convergence that ultimately leads to higher peak vertical velocities.

Both the Noah and Noah-MP experiments contain relatively high LH flux over forested regions. For the Noah LSM, the forested regions contain the highest LH values. The Noah-MP LH values are slightly lower, but the increased SH in the forested regions provides an additional forcing that helps grow convection by providing additional surface convergence and ultimately leads to higher peak vertical velocities. These conditions, along with high afternoon convective available potential energy provide more ideal conditions for cloud formation. The increased surface convergence over and adjacent to the forested areas in the Noah-MP simulation allows stronger updrafts to form in CI clouds and thus increase mass flux higher into the upper levels of the clouds.

These factors allow additional cloud graupel and ice to form and the necessary latent heating to sustain cloud growth. In contrast, the Noah experiment leads to weaker updrafts that do not sustain upper-level cloud ice, and therefore stalls cloud growth after CI occurs. This behavior provides additional evidence of the need for ice formation at the time of CI to sustain cloud growth into stronger convective storms. The sustained growth found in the Noah-MP experiment is also accompanied by increased rain at the surface. While not examined here, rainfall is essential to produce cold-pool-induced gust fronts where subsequent outflow boundary collisions may provide the uplift to trigger and sustain new convection. This can be an essential mechanism for CI across the Southeastern United States due to the prevalence of isolated convection formation resulting from enhanced convergence near outflow boundaries (Goggins et al., 2010; Wilson & Schreiber, 1986), especially when outflow boundaries collide (Harrison et al., 2009; Karan & Knupp, 2006).

Additional simulations are likely necessary to determine if the results are consistent across other parts of the United States and world. Mixed vegetation, such as those driving the results in this study, is common throughout the Southeastern United States, where strong isolated convection is frequently observed. Further, the model results are sensitive to the fraction of greenness, which directly impacts SH and LH; therefore, additional simulations examining the impacts of seasonality will be useful. The results highlight the importance of high-resolution vegetation data when assessing convective growth. Lower resolution (>5 km) studies would smooth the vegetation boundaries and likely dampen the enhanced surface convergence. Further, the findings have implications for land representation and land use change, which are difficult to assess in global model studies and highlight the importance of representing land use and vegetation change when assessing future climate studies due to the need to represent spatial heterogeneities of land vegetation and change (e.g., Clark et al., 2015; Harper et al., 2018; Vanden Broucke et al., 2015). Additional examination of the evolution of precipitation using the object-based validation methods and the extensive ground radar networks would further expand on past work relating convective growth and precipitation in NWP models (e.g., Bytheway et al., 2017).

Data Availability Statement

GOES-16 data used in this analysis can be downloaded from the National Oceanic and Atmospheric Administration Amazon Web Services (NOAA AWS; https://registry.opendata.aws/noaa-goes; NOAA GOES, 2019) data inventory. NEXRAD data provided by the NOAA National Center for Environmental Information were accessed in December 2020 (https://doi.org/10.7289/V5W9574V; NOAA National Weather Service, 1991). CAPE values were derived using the WRF-Python package (Ladwig, 2017). Simulated brightness temperature data used in

this analysis have been uploaded to a repository for archive (https://doi.org/10.5281/zenodo.6544626; Henderson et al., 2022).

Acknowledgments
The authors would like to acknowledge Sarah Griffin for providing help with the CRTM and the support of NSF Grant AGS-1746119 and AGS-1746475 to complete this work. The authors would like to thank Jonathan Case and two anonymous reviewers for their invaluable comments.

References

Anthes, R. A. (1984). Enhancement of convective precipitation by mesoscale variations in vegetative covering in semiarid regions. *Journal of Applied Meteorology and Climatology*, *23*(4), 541–554. https://doi.org/10.1175/1520-0450(1984)023<0541:eocpbm>2.0.co;2

Asefi-Najafabady, S., Knupp, K., Mecikalski, J. R., & Welch, R. M. (2012). Radar observations of mesoscale circulations induced by a small lake under varying synoptic-scale flows. *Journal of Geophysical Research*, *117*, D01106. https://doi.org/10.1029/2011jd016194

Avissar, R., & Pielke, R. A. (1991). The impact of plant stomatal control on mesoscale atmospheric circulations. *Journal of Agricultural Meteorology*, *54*, 353–372.

Avissar, R., & Schmidt, T. (1998). An evaluation of the scale at which ground-surface heat flux patchiness affects the convective boundary layer using large-eddy simulations. *Journal of the Atmospheric Sciences*, *55*, 2666–2689. https://doi.org/10.1175/1520-0469(1998)055<2666:aeotsa>2.0.co;2

Barlage, M., Chen, F., Tewari, M., Ikeda, K., Gochis, D., Dudhia, J., et al. (2010). Noah land surface model modifications to improve snowpack prediction in the Colorado Rocky Mountains. *Journal of Geophysical Research*, *115*, D22101. https://doi.org/10.1029/2009JD013470

Bikos, D., Lindsey, D. T., Otkin, J. A., Sieglaff, J., Grasso, L., Siewart, C., et al. (2012). Synthetic satellite imagery for real-time high resolution model evaluation. *Weather and Forecasting*, *27*, 784–795. https://doi.org/10.1175/waf-d-11-00130.1

Brown, M. E., & Arnold, D. L. (1998). Land–surface–atmosphere interactions associated with deep convection in Illinois. *International Journal of Climatology*, *18*, 1637–1653. https://doi.org/10.1002/(sici)1097-0088(199812)18:15<1637::aid-joc336>3.0.co;2-u

Bytheway, J. L., Kummerow, C. D., & Alexander, C. (2017). A features-based assessment of the evolution of warm season precipitation forecasts from the HRRR model over three years of development. *Weather and Forecasting*, *32*, 1841–1856. https://doi.org/10.1175/waf-d-17-0050.1

Carleton, A. M., Travis, D. J., Adegoke, J. O., Arnold, D. L., & Curran, S. (2008). Synoptic circulation and land surface influences on convection in the Midwest U.S. "Corn Belt" during the summers of 1999 and 2000. Part II: Role of vegetation boundaries. *Journal of Climate*, *21*, 3617–3641. https://doi.org/10.1175/2007jcli1584.1

Case, J. L., Crosson, W. L., Kumar, S. V., Lapenta, W. M., & Peters-Lidard, C. D. (2008). Impacts of high-resolution land surface initialization on regional sensible weather forecasts from the WRF model. *Journal of Hydrometeorology*, *9*(6), 1249–1266. https://doi.org/10.1175/2008jhm990.1

Cintineo, J. L., Pavolonis, M. J., Sieglaff, J. M., Cronce, L., & Brunner, J. (2020). NOAA ProbSevere v2.0—ProbHail, ProbWind, and ProbTor. *Weather and Forecasting*, *35*, 1523–1543. https://doi.org/10.1175/waf-d-19-0242.1

Clark, M. P., Fan, Y., Lawrence, D. M., Adam, J. C., Bolster, D., Gochis, D. J., et al. (2015). Improving the representation of hydrologic processes in Earth System Models. *Water Resources Research*, *51*(8), 5929–5956. https://doi.org/10.1002/2015wr017096

Coniglio, M. C., Correia, J., Jr., Marsh, P. T., & Kong, F. (2013). Verification of convection-allowing WRF model forecasts of the planetary boundary layer using sounding observations. *Weather and Forecasting*, *28*(3), 842–862. https://doi.org/10.1175/waf-d-12-00103.1

Dai, Y., Williams, I. N., & Qiu, S. (2021). Simulating the effects of surface energy partitioning on convective organization: Case study and observations in the US Southern Great Plains. *Journal of Geophysical Research: Atmospheres*, *126*, e2020JD033821. https://doi.org/10.1029/2020jd033821

Davis, C. A., Brown, B. G., Bullock, R., & Halley-Gotway, J. (2009). The method for object-based diagnostic evaluation (MODE) applied to numerical forecasts from the 2005 NSSL/SPC spring program. *Weather and Forecasting*, *24*(5), 1252–1267. https://doi.org/10.1175/2009waf2222241.1

Deng, G., Zhu, Y. J., Gong, J. D., Chen, D. H., Wobus, R., & Zhang, Z. (2016). The effects of land surface process perturbations in a Global Ensemble Forecast System. *Advances in Atmospheric Sciences*, *33*(10), 1199–1208. https://doi.org/10.1007/s00376-016-6036-8

Ding, S., Yang, P., Weng, F., Liu, Q., Han, Y., van Delst, P., et al. (2011). Validation of the community radiative transfer model. *Journal of Quantitative Spectroscopy and Radiative Transfer*, *112*, 1050–1064. https://doi.org/10.1016/j.jqsrt.2010.11.009

Duda, J., Wang, X., & Xue, M. (2017). Sensitivity of convection-allowing forecasts to land-surface model perturbations and implications for ensemble design. *Monthly Weather Review*, *145*, 2001–2025. https://doi.org/10.1175/MWR-D-16-0349.1

Ek, M. B., Mitchell, K. E., Lin, Y., Rogers, E., Grunmann, P., Koren, V., et al. (2003). Implementation of Noah land surface model advances in the National Centers for Environmental Prediction operational mesoscale Eta model. *Journal of Geophysical Research*, *108*, 8851. https://doi.org/10.1029/2002jd003296

Fiolleau, T., & Roca, R. (2013). An algorithm for the detection and tracking of tropical mesoscale convective systems using infrared images from geostationary satellite. *IEEE Transactions on Geoscience and Remote Sensing*, *51*, 4302–4315. https://doi.org/10.1109/tgrs.2012.2227762

Gambill, L. D., & Mecikalski, J. R. (2011). A satellite-based summer convective cloud frequency analysis over the southeastern United States. *Journal of Applied Meteorology and Climatology*, *50*, 1756–1769. https://doi.org/10.1175/2010jamc2559.1

García-García, A., Cuesta-Valero, F. J., Beltrami, H., González-Rouco, F., & García-Bustamante, E. (2021). WRF v. 3.9 sensitivity to land surface model and horizontal resolution changes over North America. *Geoscientific Model Development Discussions*, 1–32.

Goggins, G. D., Grantham, M. L., Unger, S. W., Laws, K. B., Pence, K. L., & Dawson, L. (2010). Analysis of summer convection over central Alabama. Preprints, 15th Symp. on Meteorological Observation and Instrumentation. Atlanta, GA, Amer. Meteor. Soc, 9.2.

Gravelle, C. M., Mecikalski, J. R., Line, W. E., Bedka, K. M., Petersen, R. A., Sieglaff, J. M., et al. (2016). Demonstration of a GOES-R satellite convective toolkit to ''bridge the gap'' between severe weather watches and warnings: An example from the 20 May 2013 Moore, Oklahoma, tornado outbreak. *Bulletin of the American Meteorological Society*, *97*, 69–84.

Griffin, S. M., Otkin, J. A., Nebuda, S. E., Jensen, T. L., Skinner, P. S., Gilleland, E., et al. (2021). Evaluating the impact of planetary boundary layer, land surface model, and microphysics parameterization schemes on cold cloud objects in simulated GOES-16 brightness temperatures. *Journal of Geophysical Research: Atmospheres*, *126*, e2021JD034709. https://doi.org/10.1029/2021jd034709

Griffin, S. M., Otkin, J. A., Rozoff, C. M., Sieglaff, J. M., Cronce, L. M., & Alexander, C. R. (2017). Methods for comparing simulated and observed satellite infrared brightness temperatures and what do they tell us? *Weather and Forecasting*, *32*, 5–25. https://doi.org/10.1175/waf-d-16-0098.1

Harper, A. B., Powell, T., Cox, P. M., House, J., Huntingford, C., Lenton, T. M., et al. (2018). Land-use emissions play a critical role in land-based mitigation for Paris climate targets. *Nature Communications*, *9*, 2938. https://doi.org/10.1038/s41467-018-05340-z

Harris, R. J., Mecikalski, J. R., MacKenzie, W. M., Durkee, P. A., & Nielsen, K. E. (2010). The definition of GOES infrared lightning initiation interest fields. *Journal of Applied Meteorology and Climatology*, *49*, 2527–2543.

Harrison, S. J., Mecikalski, J. R., & Knupp, K. R. (2009). Analysis of outflow boundary collisions in north-central Alabama. *Weather and Forecasting*, *24*, 1680–1690. https://doi.org/10.1175/2009waf2222268.1

Henderson, D. S., Kummerow, C. D., & Berg, W. (2018). ENSO influence on TRMM tropical oceanic precipitation characteristics and rain rates. *Journal of Climate*, *31*(10), 3979–3998. https://doi.org/10.1175/jcli-d-17-0276.1

Henderson, D. S., Otkin, J. A., & Mecikalski, J. R. (2021). Evaluating convective initiation in high-resolution numerical weather prediction models using GOES-16 infrared brightness temperatures. *Monthly Weather Review*, *149*(4), 1153–1172. https://doi.org/10.1175/mwr-d-20-0272.1

Henderson, D. S., Otkin, J. A., & Mecikalski, J. R. (2022). GOES-16 simulated BTs over the Southeastern US. [Dataset]. Zenodo. https://doi.org/10.5281/zenodo.6544626

Hong, S.-Y., Noh, Y., & Dudhia, J. (2006). A new vertical diffusion package with an explicit treatment of entrainment processes. *Monthly Weather Review*, *134*, 2318–2341. https://doi.org/10.1175/mwr3199.1

Iacono, M. J., Delamere, J. S., Mlawer, E. J., Shephard, M. W., Clough, S. A., & Collins, W. D. (2008). Radiative forcing by long-lived greenhouse gases: Calculations with the AER radiative transfer models. *Journal of Geophysical Research*, *113*, D13103. https://doi.org/10.1029/2008jd009944

Kain, J. S., Coauthors, M. C., Correia, J., Clark, A. J., Marsh, P. T., Ziegler, C. L., et al. (2013). A feasibility study for probabilistic convection initiation forecasts based on explicit numerical guidance. *Bulletin of the American Meteorological Society*, *94*, 1213–1225. https://doi.org/10.1175/bams-d-11-00264.1

Karan, H., & Knupp, K. (2006). Mobile Integrated Profiler System (MIPS) observations of low-level convergent boundaries during IHOP. *Monthly Weather Review*, *134*, 92–112. https://doi.org/10.1175/mwr3058.1

Kirkpatrick, C., McCaul, E. W., Jr., & Cohen, C. (2011). Sensitivities of simulated convective storms to environmental CAPE. *Monthly Weather Review*, *139*(11), 3514–3532. https://doi.org/10.1175/2011mwr3631.1

Kirshbaum, D. J., Fabry, F., & Cazenave, Q. (2016). The Mississippi Valley convection minimum on summer afternoons: Observations and numerical simulations. *Monthly Weather Review*, *144*, 263–272. https://doi.org/10.1175/mwr-d-15-0238.1

Knist, S., Goergen, K., & Simmer, C. (2020). Effects of land surface inhomogeneity on convection-permitting WRF simulations over central Europe. *Meteorology and Atmospheric Physics*, *132*, 53–69. https://doi.org/10.1007/s00703-019-00671-y

Ladwig, W. (2017). wrf-python. [Software]. UCAR/NCAR. https://wrf-python.readthedocs.io

Lareau, N. P. (2020). Subcloud and cloud-base latent heat fluxes during shallow cumulus convection. *Journal of the Atmospheric Sciences*, *77*(3), 1081–1100. https://doi.org/10.1175/jas-d-19-0122.1

Lawson, J. R., Kain, J. S., Yussouf, N., Dowell, D. C., Wheatley, D. M., Knopfmeier, K. H., & Jones, T. A. (2018). Advancing from convection-allowing NWP to Warn-on-forecast: Evidence of progress. *Weather and Forecasting*, *33*, 599–607. https://doi.org/10.1175/waf-d-17-0145.1

Lebo, Z. J., & Morrison, H. (2015). Effects of horizontal and vertical grid spacing on mixing in simulated squall lines and implications for convective strength and structure. *Monthly Weather Review*, *143*(11), 4355–4375. https://doi.org/10.1175/mwr-d-15-0154.1

LeMone, M. A. (1973). The structure and dynamics of horizontal roll vortices in the planetary boundary layer. *Journal of the Atmospheric Sciences*, *30*, 1077–1091. https://doi.org/10.1175/1520-0469(1973)030<1077:tsadoh>2.0.co;2

Li, X., Mecikalski, J. R., Otkin, J. A., Henderson, D. S., & Srikishen, J. (2022). A polarimetric radar operator and application for convective storm simulation. *Atmosphere*, *13*(5), 645. https://doi.org/10.3390/atmos13050645

Lim, K.-S. S., & Hong, S.-Y. (2010). Development of an effective double-moment cloud microphysics scheme with prognostic cloud condensation nuclei (CCN) for weather and climate models. *Monthly Weather Review*, *138*, 1587–1612. https://doi.org/10.1175/2009mwr2968.1

Mecikalski, J., Mackenzie, W. M., Koenig, M., & Muller, S. (2010). Cloud-top properties of growing cumulus prior to convective initiation as measured by Meteosat Second Generation. Part I: Infrared fields. *Journal of Applied Meteorology and Climatology*, *49*, 521–534.

Mecikalski, J. R., & Bedka, K. M. (2006). Forecasting convective initiation by monitoring the evolution of moving cumulus in daytime GOES imagery. *Monthly Weather Review*, *134*, 49–78. https://doi.org/10.1175/mwr3062.1

Mecikalski, J. R., Jewett, C. P., Apke, J. M., & Carey, L. D. (2016). Analysis of cumulus cloud updrafts as observed with 1-min resolution super rapid scan GOES imagery. *Monthly Weather Review*, *144*, 811–830. https://doi.org/10.1175/mwr-d-14-00399.1

Mecikalski, J. R., Williams, J. K., Jewett, C. P., Ahijevych, D., LeRoy, A., & Walker, J. R. (2015). Probabilistic 0–1-h convective initiation nowcasts that combine geostationary satellite observations and numerical weather prediction model data. *Journal of Applied Meteorology and Climatology*, *54*, 1039–1059. https://doi.org/10.1175/jamc-d-14-0129.1

Miller, P. W., & Mote, T. L. (2017). A climatology of weakly forced and pulse thunderstorms in the southeast United States. *Journal of Applied Meteorology and Climatology*, *56*, 3017–3033. https://doi.org/10.1175/JAMC-D-17-0005.1

Morrison, H., Tessendorf, S. A., Ikeda, K., & Thompson, G. (2012). Sensitivity of a simulated midlatitude squall line to parameterization of raindrop breakup. *Monthly Weather Review*, *140*(8), 2437–2460. https://doi.org/10.1175/mwr-d-11-00283.1

Murdzek, S. S., Richardson, Y. P., Markowski, P. M., & Kumjian, M. R. (2022). How the environmental lifting condensation level affects the sensitivity of simulated convective storm cold pools to the microphysics parameterization. *Monthly Weather Review* (published online ahead of print 2022). https://doi.org/10.1175/mwr-d-21-0258.1

Nakanishi, M., & Niino, H. (2004). An improved Mellor-Yamada level-3 model with condensation physics: Its design and verification. *Boundary-Layer Meteorology*, *112*, 1–31. https://doi.org/10.1023/b:boun.0000020164.04146.98

Nakanishi, M., & Niino, H. (2009). Development of an improved turbulence closure model for the atmospheric boundary layer. *Journal of the Meteorological Society of Japan*, *87*, 895–912. https://doi.org/10.2151/jmsj.87.895

Niu, G.-Y., Yang, Z. L., Mitchell, K. E., Chen, F., Ek, M. B., Barlage, M., et al. (2011). The community Noah land surface model with multiparameterization options (Noah-MP): 1. Model description and evaluation with local-scale measurements. *Journal of Geophysical Research*, *116*. https://doi.org/10.1029/2010jd015139

NOAA Geostationary Operational Environmental Satellites (GOES). (2019). NOAA Geostationary Operational Environmental Satellites (GOES) 16, 17, & 18. [Dataset]. NOAA. Retrieved from https://registry.opendata.aws/noaa-goes

NOAA National Weather Service (NWS). (1991). Radar operations center NOAA next generation radar (NEXRAD) level 2 data. NOAA National Centers for Environmental Information. [Dataset]. NWS. https://doi.org/10.7289/V5W9574V

Orth, R., Dutra, E., & Pappenberger, F. (2016). Improving weather predictability by including land surface model parameter uncertainty. *Monthly Weather Review*, *144*, 1551–1569. https://doi.org/10.1175/mwr-d-15-0283.1

Otkin, J. A., Posselt, D. J., Olson, E. R., Huang, H.-L., Davies, J. E., Li, J., & Velden, C. S. (2007). Mesoscale numerical weather prediction models used in support of infrared hyperspectral measurements simulation and product algorithm development. *Journal of Atmospheric and Oceanic Technology*, *24*, 585–601. https://doi.org/10.1175/jtech1994.1

PaiMazumder, D., Henderson, D., & Mölders, N. (2012). Evaluation of WRF-forecasts over Siberia: Air mass formation, clouds and precipitation. *The Open Atmospheric Sciences Journal*, *6*, 93–110. https://doi.org/10.2174/1874282301206010093

Patou, M., Vidot, J., Riédi, J., Penide, G., & Garrett, T. J. (2018). Prediction of the onset of heavy rain using SEVIRI cloud observations. *Journal of Applied Meteorology and Climatology*, *57*, 2343–2361.

Pei, L., Moore, N., Zhong, S., Luo, L., Hyndman, D. W., Heilman, W. E., & Gao, Z. (2014). WRF model sensitivity to land surface model and cumulus parameterization under short-term climate extremes over the southern Great Plains of the United States. *Journal of Climate*, *27*(20), 7703–7724. https://doi.org/10.1175/jcli-d-14-00015.1

Pielke, R. A. (2001). Influence of the spatial distribution of vegetation and soils on the prediction of cumulus Convective rainfall. *Reviews of Geophysics*, *39*(2), 151–177. https://doi.org/10.1029/1999rg000072

Powers, J. G., Klemp, J. B., Skamarock, W. C., Davis, C. A., Dudhia, J., Gill, D. O., et al. (2017). The weather research and forecasting model: Overview, system efforts, and future directions. *Bulletin of the American Meteorological Society*, *98*(8), 1717–1737. https://doi.org/10.1175/bams-d-15-00308.1

Qiu, S., & Williams, I. N. (2020). Observational evidence of state-dependent positive and negative land surface feedback on afternoon deep convection over the Southern Great Plains. *Geophysical Research Letters*, *47*, e2019GL086622. https://doi.org/10.1029/2019gl086622

Rickenbach, T. M., Ferreira, R. N., & Wells, H. (2020). Springtime onset of isolated convection precipitation across the southeastern United States: Framework and regional evolution. *Monthly Weather Review*, *148*, 891–906. https://doi.org/10.1175/mwr-d-19-0279.1

Santanello, J. A., Dirmeyer, P. A., Ferguson, C. R., Findell, K. L., Tawfik, A. B., Berg, A., et al. (2018). Land-atmosphere interactions: The LoCo perspective. *Bulletin of the American Meteorological Society*, *99*, 1253–1272.

Schmit, T. J., Griffith, P., Gunshor, M. M., Daniels, J. M., Goodman, S. J., & Lebair, W. J. (2017). A closer look at the ABI on the GOES-R series. *Bulletin of the American Meteorological Society*, *98*, 681–698. https://doi.org/10.1175/bams-d-15-00230.1

Senf, F., & Deneke, H. (2017). Satellite-based characterization of convective growth and glaciation and its relationship to precipitation formation over central Europe. *Journal of Applied Meteorology and Climatology*, *56*, 1827–1845. https://doi.org/10.1175/jamc-d-16-0293.1

Sutton, C., Hamill, T. M., & Warner, T. T. (2006). Will perturbing soil moisture improve warm-season ensemble forecasts? A proof of concept. *Monthly Weather Review*, *134*, 3174–3189. https://doi.org/10.1175/mwr3248.1

Thompson, G., Field, P. R., Rasmussen, R. M., & Hall, W. D. (2008). Explicit forecasts of winter precipitation using an improved bulk microphysics scheme. Part II: Implementation of a new snow parameterization. *Monthly Weather Review*, *136*, 5095–5115. https://doi.org/10.1175/2008mwr2387.1

Thompson, G., Tewari, M., Ikeda, K., Tessendorf, S., Weeks, C., Otkin, J. A., & Kong, F. (2016). Explicitly-coupled cloud physics and radiation parameterizations and subsequent evaluation in WRF high-resolution convective forecasts. *Atmospheric Research*, *168*, 92–104. https://doi.org/10.1016/j.atmosres.2015.09.005

Tiedtke, M. (1989). A comprehensive mass flux scheme for cumulus parameterization in large–scale models. *Monthly Weather Review*, *117*, 1779–1800. https://doi.org/10.1175/1520-0493(1989)117<1779:acmfsf>2.0.co;2

Trier, S. B., Chen, F., & Manning, K. W. (2004). A study of convection initiation in a mesoscale model using high-resolution land surface initial conditions. *Monthly Weather Review*, *132*, 2954–2976. https://doi.org/10.1175/mwr2839.1

Vanden Broucke, S., Luyssaert, S., Davin, E. L., Janssens, I., & van Lipzig, N. (2015). New insights in the capability of climate models to simulate the impact of LUC based on temperature decomposition of paired site observations. *Journal of Geophysical Research: Atmospheres*, *120*, 5417–5436. https://doi.org/10.1002/2015jd023095

Van Weverberg, K., Morcrette, C. J., Petch, J., Klein, S. A., Ma, H.-Y., Zhang, C., et al. (2018). CAUSES: Attribution of surface radiation biases in NWP and climate models near the U.S. Southern Great Plains. *Journal of Geophysical Research: Atmospheres*, *123*, 3612–3644. https://doi.org/10.1002/2017jd027188

Vila, D. A., Machado, L. A. T., Laurent, H., & Velasco, I. (2008). Forecast and tracking the evolution of cloud clusters (ForTraCC) using satellite infrared imagery: Methodology and validation. *Weather and Forecasting*, *23*, 233–245. https://doi.org/10.1175/2007waf2006121.1

Walker, J. R., Mecikalski, J. R., Knupp, K. R., & MacKenzie, W. M., Jr. (2009). Development of a land surface heating index-based method to locate regions of potential mesoscale circulation formation. *Journal of Geophysical Research*, *114*, D16112. https://doi.org/10.1029/2009jd011853

Weaver, C. P. (2004). Coupling between large-scale atmospheric processes and mesoscale land–atmosphere interactions in the U.S. Southern Great Plains during Summer. Part I: Case Studies. *Journal of Hydrometeorology*, *5*(6), 1223–1246.

Weckwerth, T. M., & Parsons, D. B. (2006). A review of convective initiation and motivation for IHOP_2002. *Monthly Weather Review*, *134*, 5–22. https://doi.org/10.1175/mwr3067.1

Wilson, J. W., & Schreiber, W. E. (1986). Initiation of convective storms by radar-observed boundary layer convergent lines. *Monthly Weather Review*, *114*, 2516–2536. https://doi.org/10.1175/1520-0493(1986)114<2516:iocsar>2.0.co;2

Zhang, C., Wang, Y., & Hamilton, K. (2011). Improved representation of boundary layer clouds over the southeast Pacific in ARW–WRF using a modified Tiedtke cumulus parameterization scheme. *Monthly Weather Review*, *139*, 3489–3513. https://doi.org/10.1175/mwr-d-10-05091.1

Zhang, Y., & Klein, S. A. (2010). Mechanisms affecting the transition from shallow to deep convection over land: Inferences from observations of the diurnal cycle collected at the ARM Southern Great Plains site. *Journal of the Atmospheric Sciences*, *67*, 2943–2959. https://doi.org/10.1175/2010jas3366.1

Zhu, J., Kong, F., Hu, X.-M., Guo, Y., Ran, L., & Lei, H. (2018). Impact of soil moisture uncertainty on summertime short-range ensemble forecasts. *Advances in Atmospheric Sciences*, *35*(7), 839–852. https://doi.org/10.1007/s00376-017-7107-1

Zipser, E. J. (2003). Some views on "hot towers" after 50 years of tropical field programs and two years of TRMM data. Cloud Systems, Hurricanes, and the Tropical Rainfall Measuring Mission (TRMM). *Meteorological Monographs*, *51*, 49–58. https://doi.org/10.1007/978-1-878220-63-9_5